Taylor & Francis
Taylor & Francis Group

Indole-3-lactic acid suppresses colorectal cancer via metabolic reprogramming

Shizhen Zhou [a,b]*, Kai Wang[b,c]*, Jiandong Huang[d]*, Zhen Xu[b], Qinggang Yuan[e], Lixiang Liu[a], Zhifeng Wang[d], Ji Miao[a], Hao Wang[a], Tingting Wang[b], Wenxian Guan[a,c], and Chao Ding[a]

[a]Department of General Surgery, Nanjing Drum Tower Hospital, Affiliated Hospital of Medical School, Nanjing University, Nanjing, China; [b]The State Key Laboratory of Pharmaceutical Biotechnology, Division of Immunology, Medical School, Nanjing University, Nanjing, China; [c]Department of General Surgery, Nanjing Drum Tower Hospital Clinical College of Nanjing University of Chinese Medicine, Nanjing, Jiangsu, China; [d]01life Institute, Shenzhen, China; [e]Department of Gastrointestinal Surgery, Xuzhou Central Hospital, Xuzhou, China

ABSTRACT

Research indicates that abnormal gut microbiota metabolism is linked to colorectal cancer (CRC) progression, but the role of microbiota-related tryptophan metabolism disruption remains unclear. Using metagenomic sequencing and targeted Trp metabolomics, our research identified that CRC patients had abnormal indole-3-lactic acid (ILA) levels, which were related to tumor malignancy. Exogenous ILA administration suppressed CRC development in AOM/DSS induced and xenograft mice models. Furthermore, in vitro experiments demonstrated that ILA inhibits tumor cell proliferation, migration, and anti-apoptotic capabilities. Mechanistically, ILA appears to directly occupy the phosphorylation sites of STAT3, leading to a reduction in intracellular phosphorylated STAT3 (p-STAT3) levels and the inhibition of the HK2 pathway, thereby downregulating glucose metabolism in cancer cells. Notably, this inhibition is independent of the aryl hydrocarbon receptor (AHR). In conclusion, our research findings demonstrate that alterations in tryptophan metabolism among CRC patients can influence tumor progression and reveal a novel mechanism through which ILA exerts its inhibitory effects on CRC. These findings offer new insights into the role of gut microbiota in CRC and identify potential clinical therapeutic targets.

Introduction

Colorectal cancer (CRC) ranks as the second leading cause of cancer-related mortality globally.[1,2] Current evidence unequivocally indicates that the development of CRC is accompanied by changes in the metabolism of the gut microbiota, which are believed to significantly contribute to the initiation and progression of CRC.[3–6]

Currently, a diverse array of microbial metabolites with anticancer properties has been identified, including short-chain fatty acids, amino acid derivatives, and other small-molecule metabolites.[4,6–9] Certain metabolites can increase the expression of tumor suppressor genes through the modulation of host epigenetics.[10,11] For instance, butyrate has been shown to reduce the incidence of CRC at its origin, making it an effective chemopreventive agent for CRC treatment.[12] During the progression of CRC, microbial metabolites exhibit antitumor properties by either augmenting antitumor immunity or directly inhibiting tumor cell activity.[13,14] For instance, ferrichrome, a small-molecule metabolite, has been shown to induce apoptosis in CRC cells.[15] Additionally, research has indicated that indole-3-aldehyde, an amino acid derivative, can potentiate the effectiveness of immune checkpoint inhibitors.[16] Collectively, these studies underscore the significant roles that microbial metabolites play in the initiation, progression, and treatment of CRC. Consequently, it is imperative to continue the exploration and supplementation of beneficial metabolites.

Indole-3-lactic acid (ILA) is a low-molecular-weight metabolite synthesized through the metabolic processes of the intestinal microbiota acting on tryptophan (Trp).[17] It has been identified as

a potential antitumor agent. Initial investigations into ILA have focused primarily concentrated on its role in intestinal inflammatory diseases, such as its impact on the crosstalk between the intestinal epithelium and macrophages to maintain intestinal homeostasis, ameliorate damage to the intestinal barrier, and attenuate the inflammatory response of intestinal epithelial cells.[8,18–22] The ameliorative impact on enteritis is intrinsically linked to its influence on colon cancer. Recent research has demonstrated that ILA can direct the differentiation of immature colon macrophages, thereby mitigating colitis-associated tumorigenesis.[18] Furthermore, ILA has been shown to enhance the function of CD8^{+} T cells through epigenetic mechanisms, leading to the inhibition of tumor growth.[8] In addition to augmenting antitumor immunity, ILA may have a direct inhibitory effect on tumor cells.[23,24] And the relationship between the actual levels of ILA in the intestines of patients with CRC and the severity of the tumor remains undetermined.

In this study, we elucidated the aberrant metabolism of Trp in the intestines of CRC patients and proposed a novel perspective on ILA as an inhibitor of CRC through its action on tumor cells.

Results

The content of ILA decreases in the intestine of CRC patients

To investigate the gut microbiota in CRC patients, we performed metagenomic shotgun sequencing on a total of 132 fecal samples (83 CRC patients and 49 healthy controls) (Figure 1(a)). The clinical information of all patients is given in Table S1. Following quality control filtering of the sequences (Table S2), high-quality reads were aligned to the Integrated Gene Catalog of Gut Microbes to obtain species abundance data for the samples. The alpha diversity of the gut microbiota was compared between the two groups. No significant differences were found at the species level (Figure S1A), but a decrease was detected in the CRC group at the gene level (Figure 1(c)). In this study, we analyzed gut microbiota diversity in individuals with CRC compared with healthy controls via principal coordinate analysis (PCoA) techniques. The results

showed a significant difference in microbial communities between the two groups (Figure 1(c) and Figure S1B). Additionally, linear discriminant analysis effect size (LEfSe) was used to identify variations in bacterial communities between the two groups, with a focus on assessing differences at the genus and species levels (Figure 1(d)). In conjunction with the linear discriminant analysis (LDA) score and taxonomic cladogram derived from the LEfSe analysis, our findings indicate that *Bacteroides, Proteobacteria, Enterobacterales*, and *Escherichia* were significantly more abundant in the CRC group, whereas *Clostridia, Firmicutes, Lachnospiraceae, Bifidobacterium, and Ruminococcaceae* were notably enriched in the healthy control group (Figure 1(d) and Figure S1C). In order to elucidate the microbial metabolic processes, present in CRC patients and healthy control subjects, we annotated metagenome-analyzed microbial genes within the Gut Metabolic Modules database (GMMs) (Table S3). Our analysis revealed notable alterations in Trp degradation-related metabolism (Figure 1(e)), which are in agreement with findings reported in previous studies.[24,25] Furthermore, our analysis suggested that alterations in various bacterial taxa may impact Trp metabolism, with Bacteroides being enriched in CRC patients and Clostridia and Bifidobacterium being enriched in the healthy control cohort.

Trp metabolites in CRC and healthy control feces were analyzed using targeted Trp metabolomics, which revealed 26 downstream Trp molecules, including indole derivatives and L-Kynurenine. The orthogonal partial least squares discriminant analysis (OPLS-DA) reveals notable differences in the distribution of Trp metabolites between the CRC and healthy control groups (Figure S1D). Compared with those in the healthy control group, 14 metabolites were upregulated, whereas 12 metabolites were downregulated in the CRC group (Figure 1(f) and Table S4). Among the variables under observation, fecal ILA levels were significantly lower in the CRC group than in the healthy control group (Figure 1(g)). In contrast, the fecal indoxyl sulfate (IS) levels exhibited the most pronounced increase in the CRC group, while no statistically significant differences were observed (Figure S1E). Subsequently, an
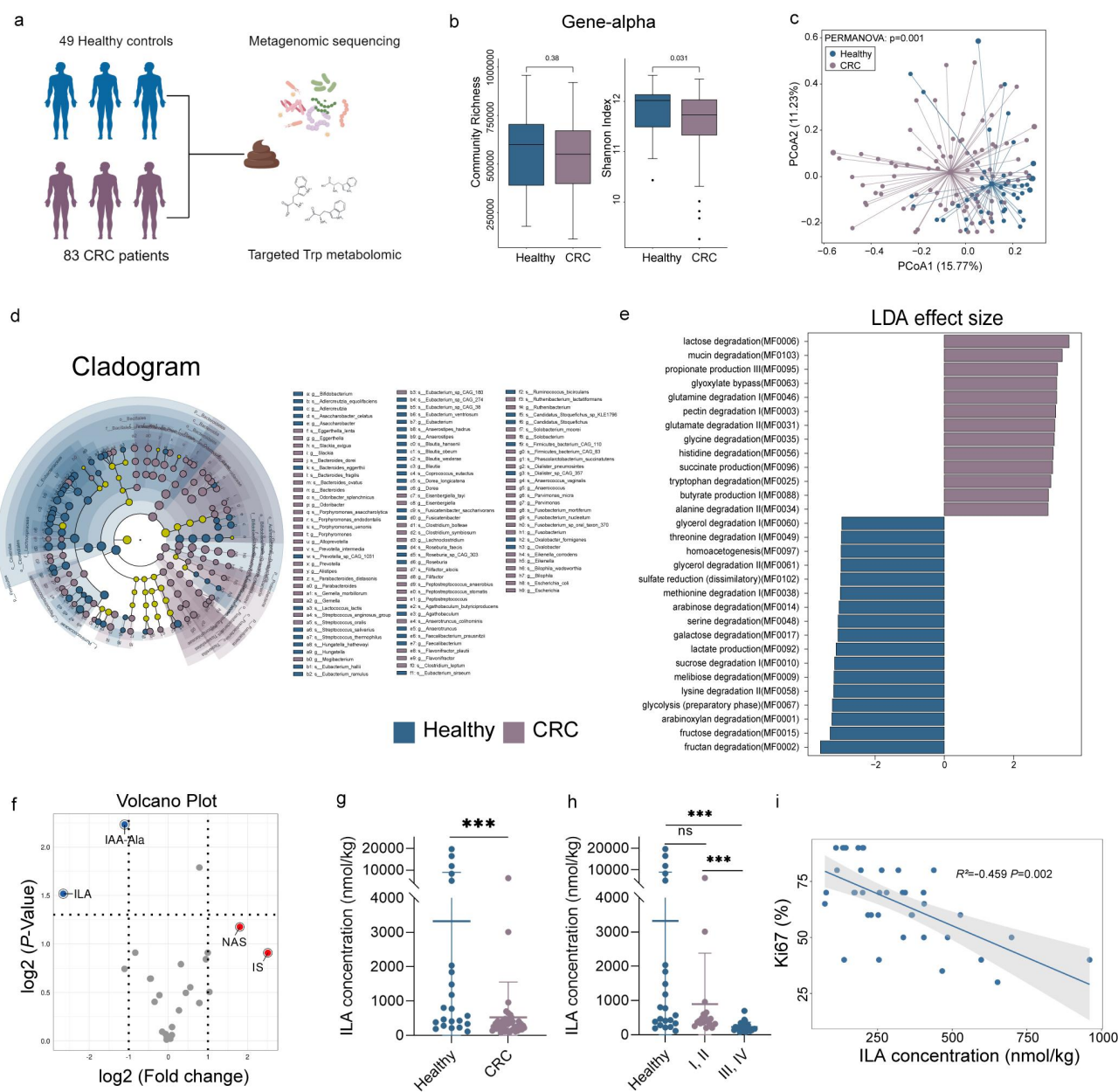
Figure 1. ILA decreases in the intestine of CRC patients. (a) Metagenomic sequencing and targeted Trp metabolomic sequencing of fecal samples obtained from a cohort of 83 CRC patients and 49 individuals without the disease serving as healthy controls. (b) Gene-based alpha-diversity (gene richness and Shannon index). (c) PCoA plot with Bray-Curtis dissimilarity at the gene level. (d) Taxonomic cladogram from LEfSe, depicting taxonomic association between microbiome communities from CRC patients and healthy control group. (e) Pathway enrichment analysis of the GMM database. (f) Representative volcano plots of major differential Trp metabolites between two groups. (g) The content of ILA in the feces of the CRC ($n = 41$) and healthy control ($n = 22$) groups. (h) According to TNM staging, CRC patients were divided into early (I, II) and late (III, IV) stages, and the content of ILA in fecal samples from each group was analyzed. (i) Spearman correlation between the amount of ILA in feces and the Ki67 ratio in colon tissues of CRC patients ($n = 35$). Data with error bars are presented as the means ± SD. Statistical significance was calculated using Wilcoxon rank-sum test (b) and Mann–Whitney U-test (g and h). $*p < 0.05$, $**p < 0.01$, $***p < 0.001$, ns: no significance. Trp: tryptophan; CRC: colorectal cancer; PCoA: Principal coordinates analysis; LEfSe: linear discriminant analysis effect size; GMM: gut metabolic module.

analysis was conducted to assess the relationships between the fecal ILA concentration and various clinical parameters. The results indicated that the level of ILA was not related to sex, age, or tumor location (Figure S1F-H). However, compared with the healthy control group and early stage patients, the level of ILA in the feces of late stage CRC patients was significantly reduced (Figure 1(h)).

Additionally, patients with poorly differentiated CRC exhibited a lower ILA content than those with medium to high differentiation, although this difference was not statistically significant (Figure S1E). Furthermore, the relationship between the ILA concentration and the tumor proliferation indicator Ki67 revealed a negative correlation ($p = 0.002$, $R^2 = -0.459$, Figure 1(i)). Our above results revealed a significant decrease in fecal ILA levels in late-stage CRC patients compared to healthy individuals. These clinical findings suggest that ILA may be a valuable metabolite for prevention and may contribute to the progression of CRC.

ILA treatment inhibits the progression of CRC in vivo

Considering the decreased content of ILA in the feces of CRC patients, particularly those in advanced stages, it is hypothesized that ILA may mitigate the progression of CRC. To investigate this hypothesis, we conducted an *in vivo* study utilizing the Azoxymethane (AOM)/Dextran Sodium Sulfate (DSS) induced tumor model, which serves as a model for inflammation-driven colorectal adenocarcinoma (Figure 2(a)). Our findings indicated that the exogenous administration of ILA resulted in a significant reduction in tumor number, size, and load (Figure 2(b,c)). Furthermore, no notable differences in mortality rates were found between the control group and the experimental group of mice during tumor progression (Figure S2A). No significant difference was observed in the efficacy of ILA supplementation via oral administration compared with that via intraperitoneal injection. Hematoxylin and Eosin (H&E) examination revealed a notable reduction in tumor-induced damage to villous structure with ILA supplementation (Figure 2(d)). Immunohistochemical analysis revealed lower positive rates of Ki67 and PCNA in ILA-supplemented tumors than in control tumors, suggesting decreased tumor cell proliferation (Figure 2(d)). Subsequently, an evaluation of innate and adaptive immune cells within colon tumors was conducted. Compared with the control group mice, ILA supplementation did not significantly change spleen weight, the proportion of tumor infiltrating macrophages, and the proportion of bone marrow-derived suppressor cells (MDSCs) (Figure 2(e) and Figure S2B-2C).

However, there was an observed increase in the proportion of tumor infiltrating CD8^{+} T cells, consistent with prior research findings (Figure 2(e) and Figure S2D).[8] These findings suggest that ILA may elicit antitumor effects by bolstering antitumor immunity or directly targeting tumor activity.

Subsequently, we assessed the anti-tumor efficacy of ILA supplementation in mice bearing unilateral tumors (MC38 cells) with intact immune function (Figure 2(f)). Consistent with previous research findings, the administration of ILA via peritumoral and intraperitoneal injection led to a notable decrease in tumor size, and no impact on the spleen weight or the body weight of the mice (Figure 2(g–i) and Figure S2E-S2F). To assess tumor progression, the mice were euthanized on the 24th day, and samples of MC38 tumor tissue samples were obtained. Immunohistochemical analysis revealed reduced expression levels of Ki67 and PCNA in the ILA-treated group (Figure 2(j)). Following ILA supplementation, there was an observed increase in the infiltration of CD8^{+}T cells into the tumor, although this difference was not found to be statistically significant (Figure 2(k)). To elucidate the role of the immune system in the anti-tumor mechanisms of ILA, we administered anti-CD8 antibodies to inhibit mouse CD8^{+} T cells. Notably, despite this intervention, ILA still effectively reduced tumor volume and weight (Figure S3A-S3C). Additionally, our experiments with nude mice bearing HCT116 tumors demonstrated that supplementation with ILA led to a reduction in tumor volume (Figure S3D-3 G), suggesting that ILA can elicit antitumor effects through mechanisms independent of CD8^{+}T cells. In summary, our results showed that ILA supplementation inhibits CRC progression *in vivo*. The efficacy of ILA in reducing tumor volume has been demonstrated in several mouse models, suggesting potential mechanisms beyond CD8^{+} T cell involvement.

ILA treatment inhibits the viability of CRC cells

To investigate the potential direct effects of ILA on tumor cells, functional analyses were conducted *in vitro* using two CRC cell lines, MC38 and HCT116. Coculturing ILA with the CRC cell lines at various concentrations and durations revealed that ILA inhibited the proliferation of CRC cells, as evidenced by CCK8 and EdU tests after 48 hours, in
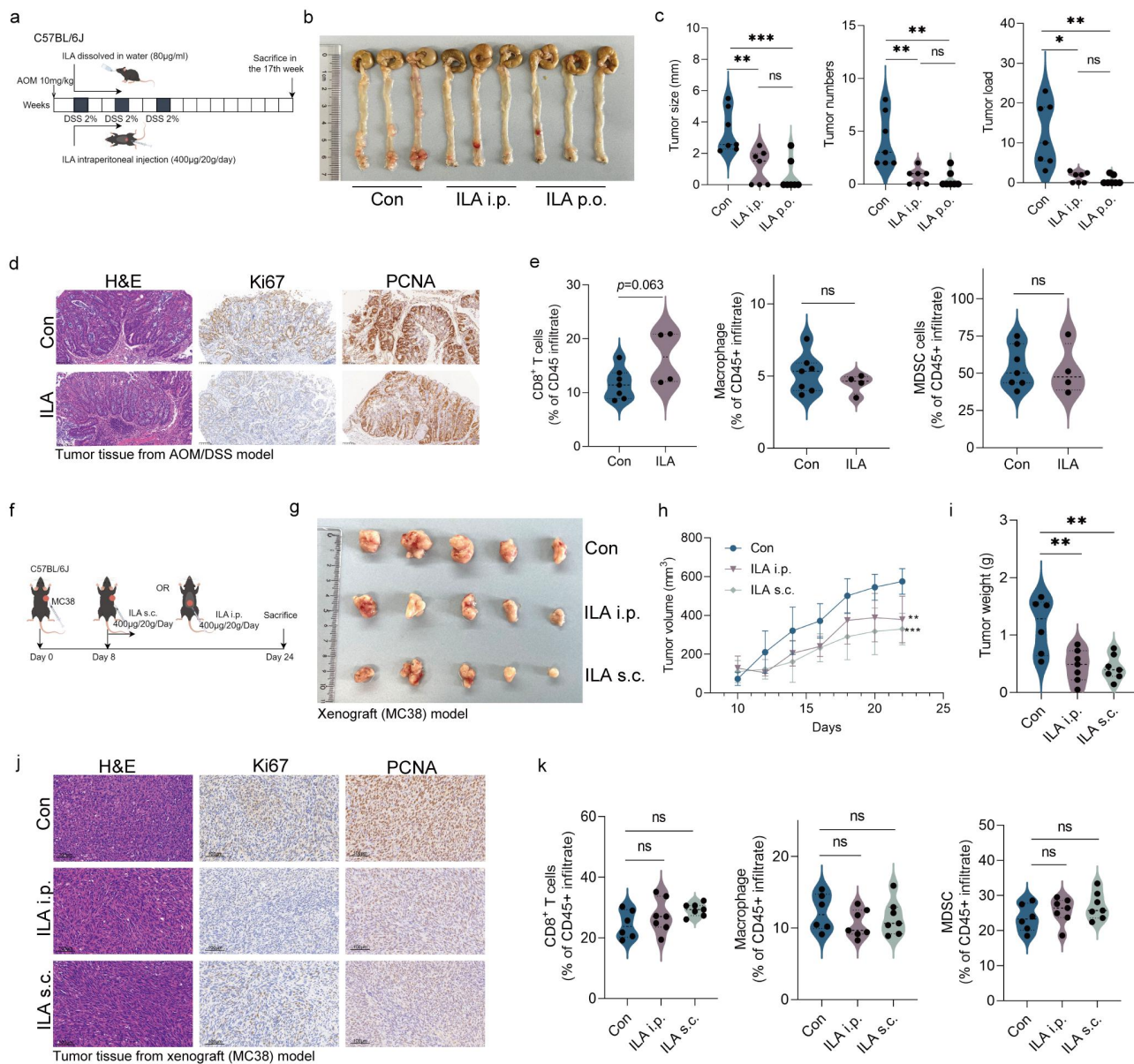
Figure 2. ILA suppresses tumor progression *in vivo*. (a) Schematic illustration of the administration of ILA through daily p.o. and i.p. in mice with AOM/DSS-induced colorectal cancer (*n* = 7). (b) Representative images of colon tumors were shown. (c) The tumor number, tumor size, and total tumor mass (tumor load) in each mouse were measured. (d) Colon tumors were analyzed histopathologically using H&E staining, with additional staining for Ki67 and PCNA. (e) Quantification of the relative abundances of CD8$^+$ T cells (CD3$^+$CD8$^+$), macrophages (CD11b$^+$F4/80$^+$), and myeloid-derived suppressor cells (MDSCs) (CD11b$^+$Gr1$^+$) within tumor samples through flow cytometric analysis (*n* = 4–7). (f) Experimental design for MC38 tumor-bearing in C57BL/6 mice and ILA administration schedule (*n* = 6–7). ILA i.p.: intraperitoneal injection of ILA; ILA s.c.: subcutaneous injection of ILA. (g–i) The alterations in tumor volume were assessed (h), excise the tumor 24 days post-transplantation, photographic images were captured (g), and tumor weight (i) was determined. (j) Histological analysis of colon tumors was shown by H&E staining with additional staining for Ki67 and PCNA. (k) The proportions of tumor-infiltrating CD8$^+$T cells, macrophages, and MDSCs were detected. Data with error bars are presented as the means ± SD. Violin plots represent both distribution and density of data, and statistical significance was calculated using unpaired two-tailed *t* test (e), and Mann–Whitney U-test (c, i, and k). *P < 0.05, **p < 0.01, ***p < 0.001, ns: no significance. p.o.: oral, i.p.: intraperitoneal injections; AOM: azoxymethane; DSS: dextran sulfate sodium; H&E: hematoxylin and eosin; PCNA: proliferating cell nuclear antigen; MDSC: myeloid-derived suppressor cell.

a concentration-dependent manner (Figure 3(a,b)). Additionally, colony formation experiments demonstrated that ILA can inhibit colony formation in CRC cell lines (Figure 3(c)). By using transwell assays, ILA inhibited the migration of MC38 and HCT116 cells (Figure 3(d)). Subsequently, the proportion of apoptotic cells was increased upon ILA treatment (Figure 3(e)). These results showed that ILA directly inhibited proliferation, colony formation, and migration of CRC cells in a concentration-dependent manner, indicating its potential as a therapeutic agent to inhibit cell viability and progression.
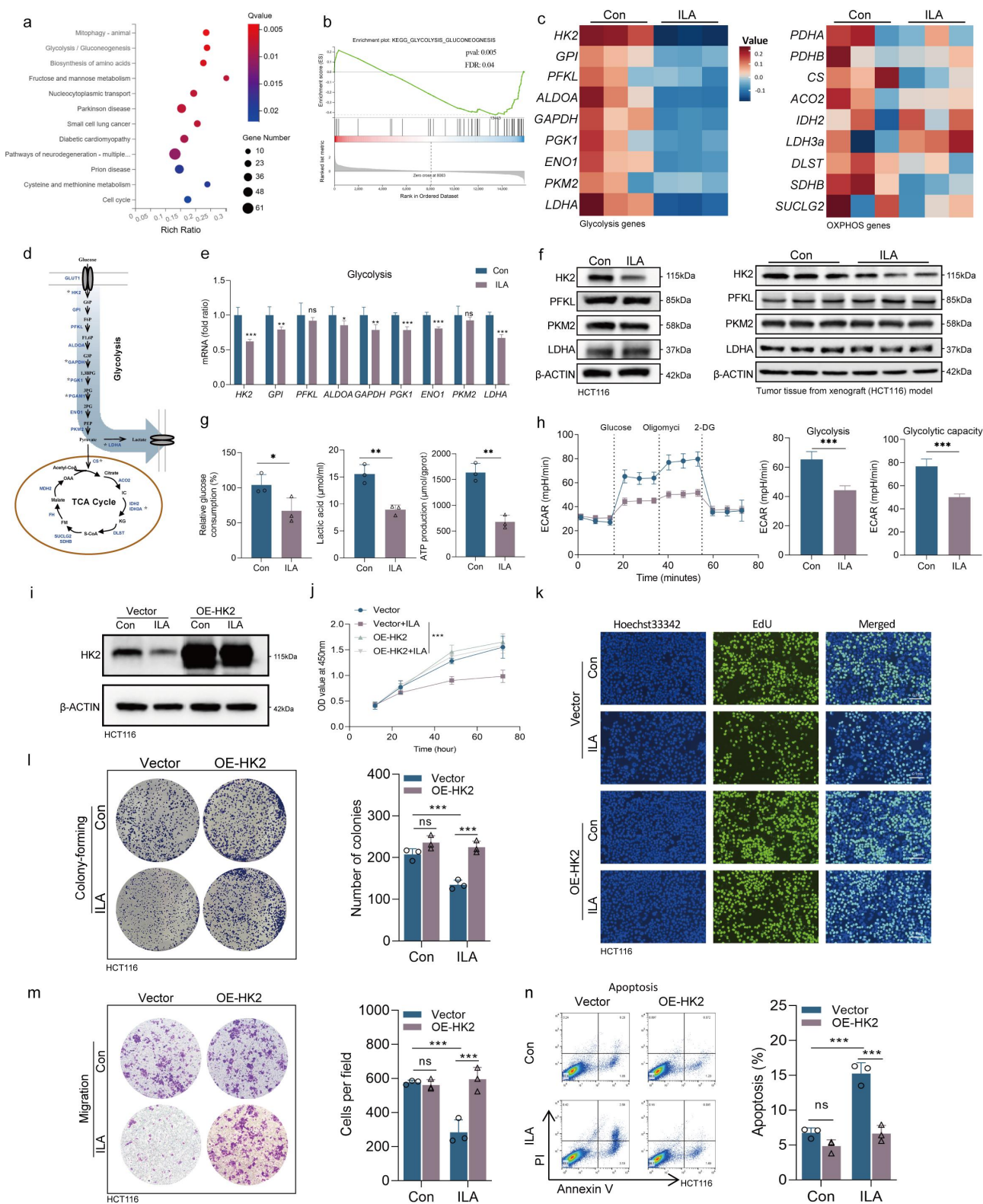
ILA treatment modulates tumor cell glycolysis by inhibiting HK2 expression

Next, to clarify how ILA inhibits the activity of CRC cells, we performed RNA-seq analysis on the CRC cell line HCT116 cocultured with ILA. After ILA stimulation, 744 genes were downregulated, whereas 650 genes were upregulated in HCT116 cells (Table S5). We conducted gene enrichment analysis and found that the genes whose expression changed were enriched mainly in the glycolytic pathway (Figure 4 (a,b)). The Warburg effect in tumor cells is related to impaired mitochondrial oxidative phosphorylation,
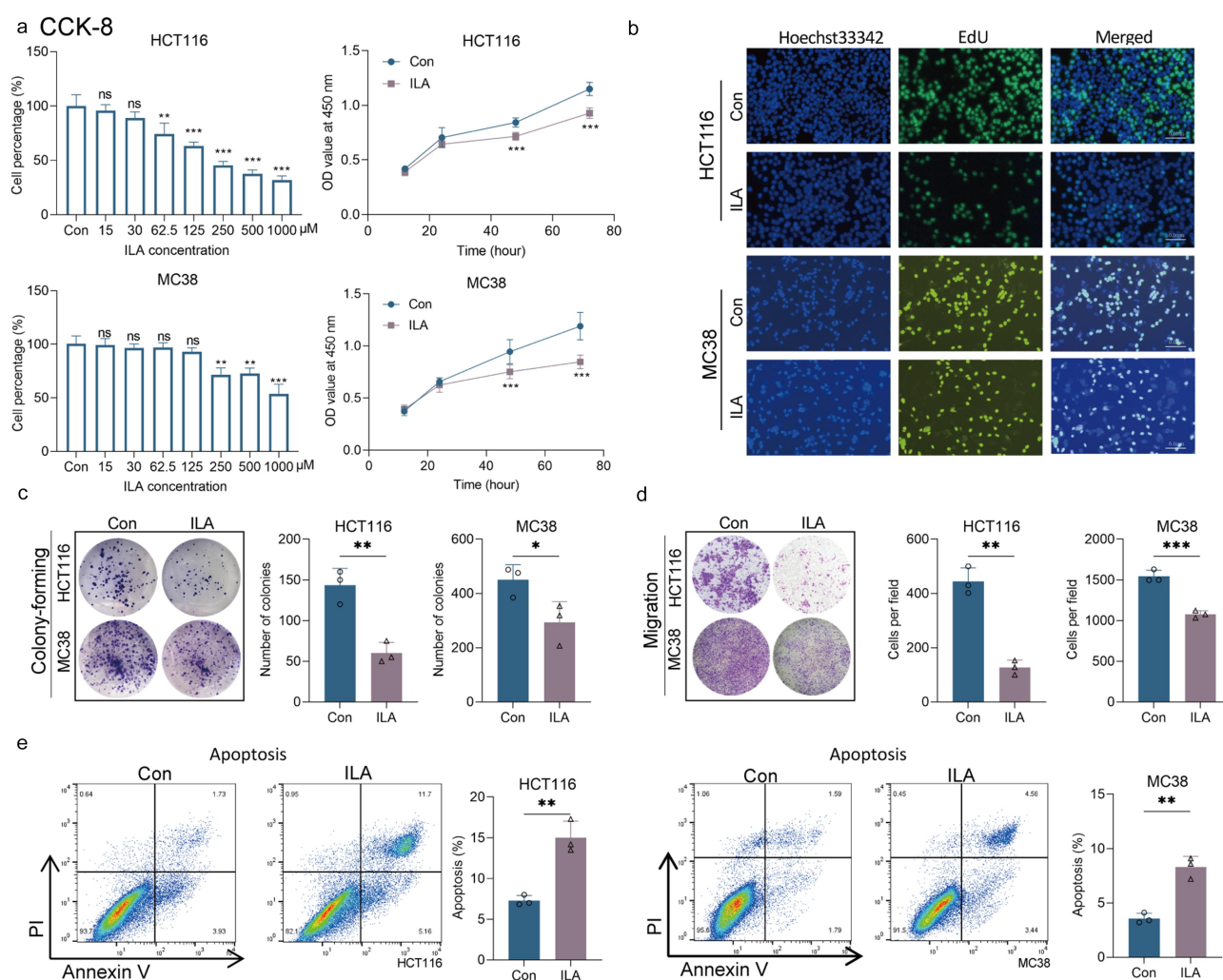
Figure 3. ILA inhibits the viability of colorectal cancer cells *in vitro*. (a) The proliferation ability of HCT116 and MC38 cells after treatment with DMSO or ILA was evaluated at different concentrations and time points via the CCK8 assay ($n = 5$). (b) The EdU assay was used to assess the percentage of actively dividing cells in HCT116 and MC38 cells following 48 hours of treatment with either DMSO or ILA (250 μM). (c) The colony formation assay was employed to assess the colony-forming capacity of HCT116 and MC38 cells following exposure to either DMSO or ILA (250 μM). (d) The migratory properties of the cells were analyzed using the transwell migration assay with transwell filter chambers. (e) Apoptosis of cells treated with ILA (250 μM) was compared to that of DMSO-treated cells. Data represent are presented the means ± SD. Statistical significance was calculated using unpaired two-tailed *t* test (a, c, d, and e). *$p < 0.05$, **$p < 0.01$, ***$p < 0.001$, ns: no significance.

Figure 4. ILA modulates tumor cell glycolysis by inhibiting HK2 expression. (a–c) RNA-seq analysis of HCT116 cells treated with DMSO or ILA (250 μM) for 24 h. (a) The top 12 enrichment KEGG pathways in ILA group. (b) GESA analysis showed a decrease in glycolytic pathway enrichment after ILA treatment. (c) Heatmap depiction of the gene expression involved in glycolysis and OXPHOS. (d) Pattern diagram of major gene changes in glucose metabolism based on the RNA-seq results. (e) Application of RT-qPCR experiment to detect changes in glycolysis gene expression in HCT116 cells after ILA stimulation ($n = 3$). (f) The protein expression of HK2, PKM2, PFKL, and LDHA was detected by WB in HCT116 cells treated with DMSO or ILA, and in tumor tissue from a xenograft model of CRC. (g) HCT116 cells were treated with DMSO or ILA and lactic acid production, ATP production, and glucose consumption were detected. (h) The

abnormal expression of glucose metabolism enzymes, oncogene activation, TSG inactivation, and changes in the tumor microenvironment.[26,27] Several key glycolytic genes *HK2*, *PFKL*, *PKM2*, and *LDHA* were downregulated after ILA stimulation (Figure 4(c,d) and Figure S4A). Similar results were found in HCT116 cells using RT-qPCR (Figure 4(e)). Furthermore, Western blotting (WB) was used to detect the changes in glycolytic protein levels and subcutaneous tumor tissue after supplementation with ILA (Figure 4(f)). We found that HK2 showed the most significant changes at the mRNA and protein levels. Next, we investigated whether ILA can regulate glycolysis and oxidative phosphorylation of HCT116 cells *in vitro*. We found that after treatment with ILA, the lactate production, glucose consumption, and ATP production were reduced (Figure 4(g)). A Seahorse XFe24 extracellular flux analyzer was used to measure glucose metabolism in HCT116 cells. The results indicated that ILA significantly reduced the glycolytic level but had no effect on oxidative phosphorylation (Figure 4(h) and Figure S4B).

To validate that ILA inhibits glycolysis by suppressing the expression of HK2, we transiently increased the expression of HK2 in HCT116 cells and assessed the levels of HK2 post-enhancement using WB (Figure 4(i)). Furthermore, we conducted biological functional assays to evaluate the impact of ILA on cell activity subsequent to HK2 overexpression. The results demonstrated that the upregulation of HK2 counteracted the impact of ILA (Figure 4(j-m)). Additionally, we administered 2-deoxyglycose (2-DG) to ILA-supplemented HCT116 cells to assess changes in cell viability following glycolysis inhibition. Our results indicated that ILA did not exert additional inhibitory effects on cell viability under these conditions (Figure S4C-F). These above results show that ILA inhibits CRC cell glycolysis by suppressing HK2 expression, resulting in reduced lactate production and glucose consumption. This highlights the potential of ILA to inhibit CRC progression by targeting tumor cell metabolism.
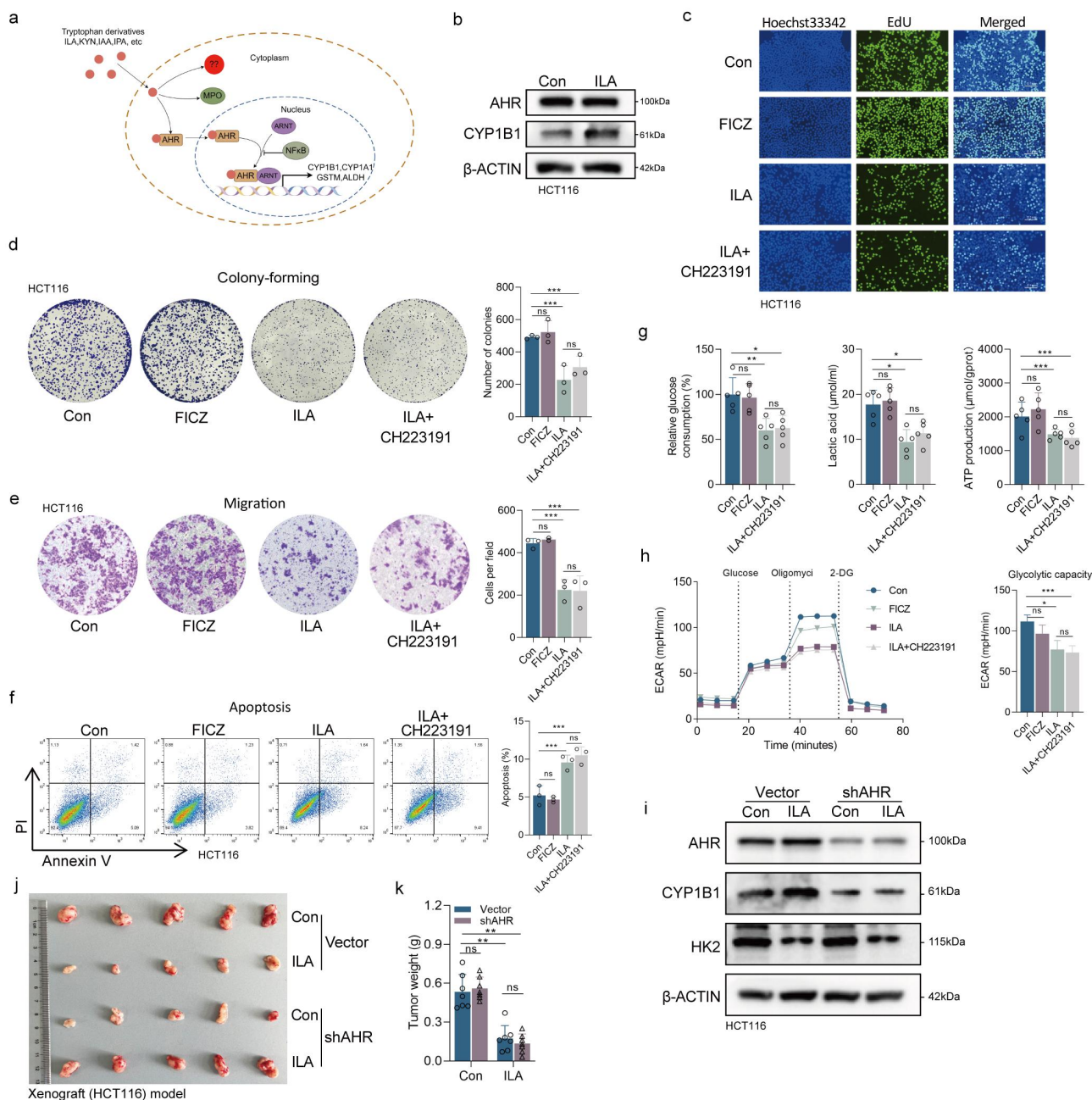
ILA reduces HK2 expression independent of AHR

As an indole derivative, ILA functions as an exogenous ligand of the aryl hydrocarbon receptor (AHR). Previous research has demonstrated the ability of ILA to activate AHR and elicit its effects, leading to speculation regarding the potential antitumor effects of ILA mediated through AHR[23,24,28–30] (Figure 5(a)). We conducted protein-level validation and observed a significant increase in the expression of AHR and CYP1B1 in HCT116 cells following stimulation with ILA (Figure 5(b)). CYP1B1, a member of the cytochrome P450 family, was identified as a marker for AHR activation.[31,32] After ILA stimulation, there was a significant increase in the nuclear displacement of AHR (Figure 5(b) and Figure S5A). To investigate the potential mechanism by which ILA inhibits tumor cell activity through inhibiting glycolysis via AHR, we utilized the AHR receptor inhibitor CH223191.[33] Surprisingly, our findings indicated that AHR inhibitors failed to rescue the inhibitory effect of ILA on cell activity (Figure 5(c-f)). Additionally, the classic ligand 6-Formylindolo[3,2-b] carbazole (FICZ) of the AHR receptor was used as a positive control, revealing its inability to inhibit tumor cell activity. AHR knockdown cell lines were generated and subsequently subjected to ILA stimulation (Figure 5(i)). Upon AHR knockdown, ILA maintained its ability to suppress the proliferation and migration of HCT116 cells, as well as its ability to induce apoptosis (Figure S5B-5E). The stable shAHR cell line was utilized in xenograft model experiments, revealing that *in vivo* AHR knockdown did not negate the inhibitory influence of ILA on tumor growth (Figure 5(j,k)). Furthermore, our investigation demonstrated that the suppression of tumor cell glycolysis by ILA was not affected by AHR receptor inhibitors (Figure 5(g,h) and Figure S5F-5 G). Our results further demonstrated that ILA reduces HK2 expression independently of the AHR pathway, as evidenced by experiments showing that AHR inhibitors and knockdown did not reverse the inhibitory

ECAR of HCT116 cells was monitored after treated with DMSO or ILA, and the levels of glycolytic capacity and glycolysis were quantified ($n = 5$). (i) WB analysis of HK2 in HCT116 cells with HK2 over-expressing. (j–k) CCK8 assay (j), EdU assay (k), colony formation (l), transwell migration assay (M), and apoptosis assay (n) verified the effect of ILA (250 μM) on the viability of HCT116 cells after over-expressing HK2. Data represent are presented the means ± SD. Statistical significance was calculated using unpaired two-tailed *t* test (e, g, h, and j), and Mann–Whitney U-test (l, m, and n). *$p < 0.05$, **$p < 0.01$, ***$p < 0.001$, ns: no significance. GSEA: gene set enrichment analysis; OXPHOS: oxidative phosphorylation; ECAR: extracellular acidification rate.

Figure 5. ILA reduces HK2 expression independent of AHR. (a) Schematic diagram illustrating some representative acting modes of Trp derivatives. (b) WB analysis of AHR and its downstream molecules was performed. (c–f) EdU assay (c), colony formation (d), transwell migration assay (e), and apoptosis (f) assays verified the effect of ILA (250 µM) on the viability of HCT116 cells cultured in the presence or absence of CH223191, an inhibitor of the AHR. FICZ was used as a positive control for AHR ligands. (g) Lactic acid production, ATP production, and glucose consumption were detected after using ILA to stimulate HCT116 cells in the presence or absence of CH223191. (h) The ECAR of HCT116 cells was monitored after treatment with ILA for 24 h in the presence or absence of CH223191, and the levels of glycolytic capacity were quantified. (i) WB analysis of AHR, CYP1B1, and HK2 in HCT116 cells with AHR knockdown. (j–k) Tumors were photographed and measured ($n = 7$). Data represent are presented the means ± SD ($n \geq 3$). Statistical significance was calculated using Mann–Whitney U-test (d–h and k). $*p < 0.05$, $**p < 0.01$, $***p < 0.001$, ns: no significance. WB: Western blotting; FICZ: 6-Formylindolo (3,2-b) carbazole.

effects of ILA on CRC cell activity and glycolysis. These results suggest that the modulation of tumor metabolism by ILA is not mediated by the AHR, highlighting a new mechanism in CRC progression.

ILA inhibits the viability of CRC cells through the p-STAT3-HK2 axis

Phosphorylation of STAT3 is necessary for its translocation from the cytoplasm to the nucleus for its functional activity.[34,35] Our investigation revealed that the expression level of STAT3 remained constant in tumor cells treated with ILA, while its phosphorylation level decreased significantly (Figure 6(a)). The phosphorylation of STAT3 predominantly takes place within the Src homology 2 (SH2, residues 584–688) domain,[36] with tyrosine 705 (Tyr705) being the most frequently modified residue.[37,38] Subsequently, the phosphorylated Tyr705 (pTyr705) interacts with the SH2 domain of the opposing STAT3 subunit, thereby facilitating STAT3 dimerization and culminating in the phosphorylation process.[35,39,40] Through molecular docking simulations, we demonstrated that ILA exhibits a strong binding affinity to the SH2 domain, forming a robust π-cation interaction with the Arg609 residue (Figure 6(b)). In contrast, the binding of pTyr705 to the SH2 domain is mediated solely by hydrogen bonds (Figure S6A). ILA competes for the SH2 docking pocket, thereby inhibiting the binding of pTyr705 to SH2 and consequently suppressing the phosphorylation process of STAT3 (Figure S6B). To further elucidate this mechanism, we utilized the online database JASPAR (http://jaspar.genereg.net/) to identify a consensus binding site for STAT3 in the HK2 promoter region, with a high score of 11 (Figure 6(c)).[41] Then chromatin immunoprecipitation quantitative polymerase chain reaction (ChIP-qPCR) analysis revealed a marked decrease in the enrichment of STAT3 at the HK2 promoter following ILA stimulation (Figure 6(d)). Furthermore, ectopic expression of STAT3 effectively counteracted the decrease in tumor cell proliferation and migration capacity, and the increase in apoptosis triggered by ILA (Figure 6(e-i)). Notably, the upregulation of STAT3 negated the suppressive effect of ILA on HK2 expression and glycolysis levels (Figure 6(j,k)).

Subsequently, the expression of HK2 and STAT3 in CRC were examined. By utilizing IHC and WB assays revealed that the expression of HK2 and STAT3 was notably upregulated in tumor tissue compared with adjacent tissues (Figure 6(m) and Figure S6C). Furthermore, analysis of the Gene Expression Omnibus (GEO) dataset (GSE24550, Table S6) corroborated the increased expression levels of HK2 and STAT3 in tumor tissues, and there was a positive correlation between their expression levels (Figure 6(m)). The same results were also obtained in the TCGA database (Figure S6D-E, Table S7). Our analysis delved deeper into the role of ILA in the context under study. The results of the WB experiment revealed a significant decrease in the expression of HK2 in the high-ILA group compared to that in the low-ILA group, as well as a notable reduction in the amount of p-STAT3 in the tumor tissue of the high-ILA group (Figure 6(n)). The quantification of HK2 protein levels in CRC tumor tissue and the subsequent analysis of its association with ILA content revealed a significant negative correlation (Figure S6F). These findings show that ILA inhibits CRC cell viability through the p-STAT3-HK2 axis by directly targeting STAT3 phosphorylation, resulting in decreased p-STAT3 enrichment at the HK2 promoter.

In conclusion, our study revealed a decrease in ILA levels in the intestines of CRC patients, which was significantly associated with tumor progression. Our findings suggest that ILA exerts a direct inhibitory effect on tumor cells by limiting their proliferation, migration, and antiapoptotic capabilities. Furthermore, our results indicate that ILA acts independently of AHR by directly inhibiting the activation of STAT3, leading to a reduction in HK2 expression and ultimately inhibiting the glycolytic pathway in tumor cells. This study provides new insights into the role of ILA in the inhibition of CRC and establishes a new theoretical basis for future research.

Discussion

This study presents novel findings suggesting a potential correlation between decreased levels of intestinal ILA in patients and CRC progression. Additionally, this study confirmed the antitumor properties of ILA through both *in vivo* and *in vitro* experiments confirmed the antitumor properties of
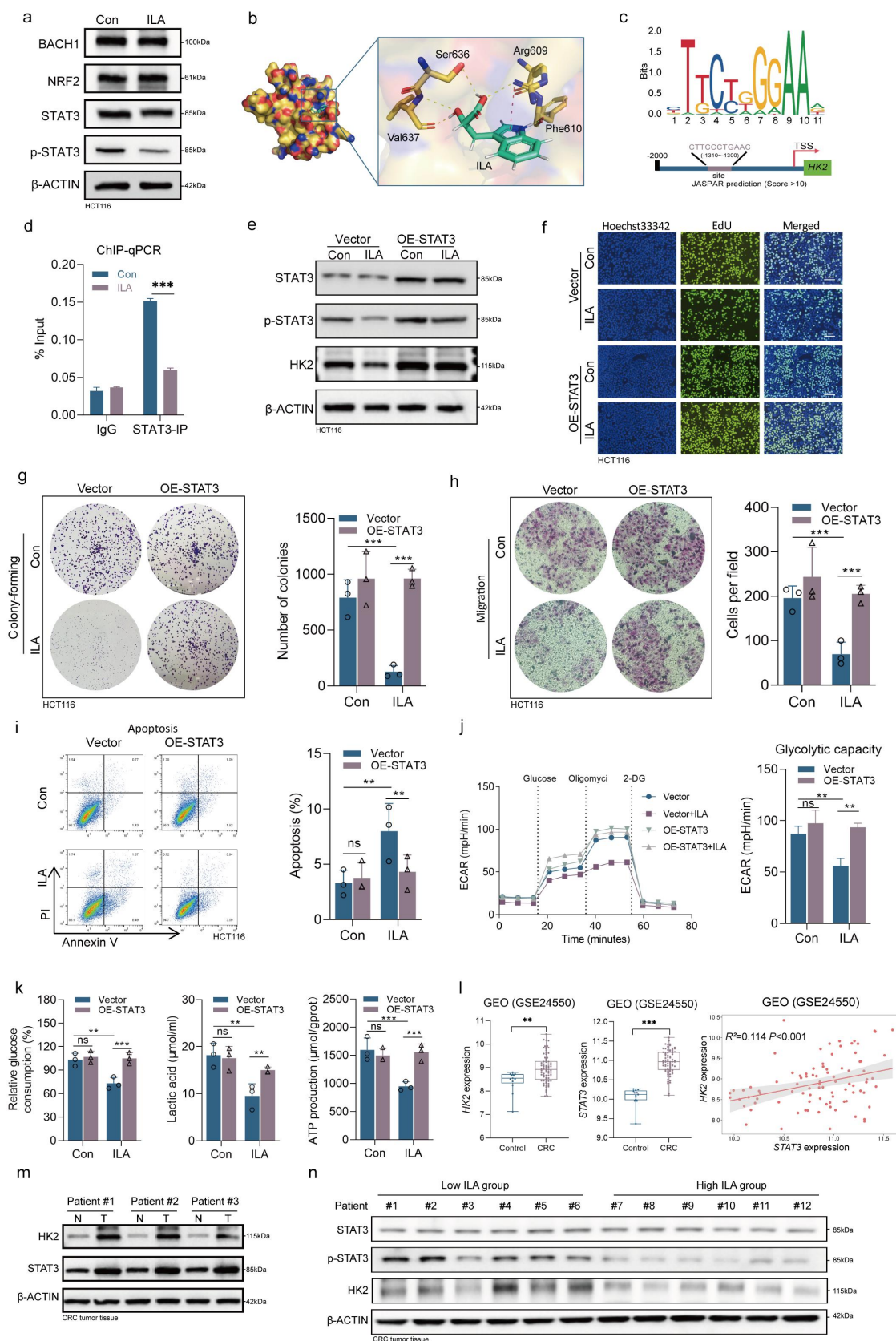
Figure 6. ILA inhibits tumor activity through the p-STAT3-HK2 axis. (a) Protein levels of the common transcription factors of HK2 in HCT116 cells after treatment with ILA (250 μM) for 24 h were detected by WB. (b) The molecular docking pattern diagram. ILA is stably located within the docking pocket, where it establishes hydrogen bonding interactions with Ser636, Arg609, Val637, and Phe610, as well as π-cation interactions with Arg609. Hydrogen bonds are indicated by yellow dashed lines, π-cation bond is denoted by red

ILA. Notably, this study proposes that ILA can directly target tumor cells, inhibiting their activity independently of antitumor immune mechanisms. Our findings indicate that ILA can inhibit the phosphorylation of STAT3 in tumor cells independently of AHR, thereby disrupting aerobic glycolysis and impeding tumor growth.

Metabolites produced by the gut microbiota have been shown to inhibit colorectal tumor growth through direct interactions with tumor cells. These interactions include promoting tumor cell apoptosis, inducing oxidative stress, and inhibiting glycolysis, among other mechanisms.[42,43] These metabolites are typically found at lower levels in patients with CRC. Our study similarly identified a deficiency of ILA in CRC patients, particularly those in advanced stages. We hypothesize that this deficiency may be related to the progression of CRC. Furthermore, both *in vivo* and *in vitro* experiments have demonstrated that supplementation with exogenous ILA can effectively inhibit the development of CRC.

Tumor progression is typically influenced by both antitumor immunity and intrinsic tumor cell activity. Prior research has indicated that ILA can stimulate anti-tumor immune responses and markedly augment the cytotoxic efficacy of CD8^{+} T cells. In the present study, utilizing an immunodeficient mouse model, we demonstrated that the tumor-inhibitory effects of ILA are not exclusively reliant on the immune system. We observed that ILA had a significant inhibitory effect on tumor cell activity. This was evidenced by a reduction in their proliferation rate and a lower resistance to apoptosis. A crucial determinant in sustaining the proliferative capacity of tumor cells is the Warburg effect, which facilitates the rapid and adequate energy supply necessary for tumor cell survival and functions as a precursor for various biosynthetic pathways.[26] Prior research has demonstrated that gut microbiota can metabolize and produce short-chain fatty acids, bile acids, and other metabolites that impact the Warburg effect in tumor cells.[44–46] We propose the hypothesis that ILA may modulate the metabolic processes of tumors. Our findings indicate that ILA can decrease ATP and lactate production in tumor cells and significantly inhibit glycolysis.[47]

Indole-3-lactic acid, a metabolic derivative of tryptophan, is a well-known exogenous ligand for AHR. Previous research on ILA has focused primarily on its AHR-mediated effects. For instance, Wang et al. demonstrated that activation of the AHR-NRF2 pathway ameliorates intestinal barrier damage.[30,48] Acting as an intracellular receptor and transcription factor, the AHR plays a critical role as a sensor for immune cells to adapt to changing environmental conditions.[31,49,50] While earlier investigations primarily concentrated on the mechanisms of action of kynurenine (KYN) and indole derivatives via AHR, emerging research has increasingly demonstrated that these metabolites can also exert their effects through AHR-independent pathways.[51] Our research suggests that the suppression of tumor cell activity by ILA is not exclusively reliant on AHR. This conclusion is supported by our experimental validation. The use of AHR inhibitors or AHR knockdown does not reduce the inhibitory effect of ILA on tumor cell activity. STAT3 is a crucial transcription factor in HK2, maintaining persistent activation in colon cancer cells.[34,52] Small-molecule inhibitors targeting STAT3 activation are regarded as effective antitumor agents.[36,38] We identified that the structure of ILA interacts with the SH2 domain of STAT3 to inhibit its activation.

---

dashed lines. (c) Schematic representation of potential sites in the promoter region of HK2 for STAT3 binding as predicted by JASPAR. (d) ChIP-qPCR was used to detect STAT3 enrichment at *HK2* promoter after treatment with ILA for 24 h. (e) The STAT3, p-STAT3, and HK2 protein levels in HCT116 cells overexpressing STAT3 were detected by WB. (f-i) EdU assay (f), colony formation (g), transwell migration (h), and apoptosis (i) assay verified the effect of ILA (250 μM) on the viability of HCT116 cells with overexpressing STAT3. (j) The ECAR was monitored and the levels of glycolytic capacity were quantified after ILA was used to stimulate HCT116 cells overexpressing STAT3. (k) Lactic acid production, ATP production, and glucose consumption were detected after ILA was used to stimulate HCT116 cells overexpressing STAT3. (l) Expression levels of HK2 and STAT3 in normal tissues and tumor tissues from CRC patients in the GEO database. Spearman correlation of the mRNA levels of *HK2* and *STAT3* in GSE24550. (m) WB was used to detect the expression levels of HK2 and STAT3 in normal tissues and tumor tissues of CRC patients. (n) The expression levels of HK2, STAT3, and p-STAT3 expression were measured in tumor tissues from CRC patients with low and high ILA levels. Data represent are presented as means ± SD ($n \geq 3$). Statistical significance was calculated using Mann–Whitney U-test (d, g-k, and k). *$p < 0.05$, **$p < 0.01$, ***$p < 0.001$, ns: no significance.

Limitations of the study

This study, based on a small single-center clinical sample, may have biases due to sample limitations. To accurately assess ILA distribution in colorectal cancer patients, future research should involve more diverse medical centers and populations. Our current understanding of ILA's role in glycolysis regulation is limited, despite some progress. We aim to explore additional molecular mechanisms and analyze ILA's impact on glycolysis from various angles to enhance the theoretical framework. While ILA shows promise in tumor inhibition, it is not yet ready for clinical use. We have not conducted clinical trials, so its effectiveness and safety in humans remain unverified.

Resource availability

Lead contact

For further information and requests for resources and reagents, please contact the lead author, Chao Ding (dingchao21@nju.edu.cn).

Materials availability

This study did not produce any novel reagents.

Data and code availability

This publication does not include any original code. The datasets generated and/or analyzed during this study are accessible through the Lead Contact for the purpose of data reanalysis. Any supplementary information necessary for reanalyzing the data presented in this paper can be obtained from the Lead Contact upon request.

Methods

Human samples

To investigate alterations in the gut microbiota and metabolites in CRC patients, fecal samples were obtained from Nanjing Drum Tower Hospital, and control samples were collected from the physical examination center of the same hospital. Inclusion criteria for the colorectal cancer cohort are as follows: (1) Participants must be aged between 18 and 80 years; (2) A confirmed diagnosis of colorectal cancer via pathological assessment, with plans for radical surgical intervention; (3)

Absence of antibiotic, microbial preparation, or corticosteroid usage within the 3 months preceding specimen collection; (4) A body mass index (BMI) within the normal range of 18.5 to 25; (5) Provision of informed consent by all participants. Exclusion criteria include (1) A history of major abdominal surgeries, with the exception of cholecystectomy and appendectomy; (2) Presence of complete intestinal obstruction; (3) Diagnosis of chronic diarrhea, inflammatory bowel disease, or other conditions known to affect gut microbiota; (4) Undergoing neoadjuvant chemoradiotherapy; (5) Severe dysfunction of the heart, brain, liver, lungs, kidneys, or other vital organs; (6) Belonging to ethnic minorities with distinct dietary practices; (7) Demonstrating poor compliance or inability to cooperate. The average age of the CRC patients was 83, whereas that of the control donors was 49. Additional clinical and pathological details of the patients are presented in Table S1.

Fecal sample collection and DNA extraction

Fecal samples were collected from all participants for metagenomic sequencing after confirming that they had not undergone antibiotic treatment for a minimum of 1 month prior to sample collection. Additionally, individuals refrained from consuming probiotic-rich foods, such as yogurt, in the week leading up to sample collection. Each sample was promptly frozen at −80℃ or temporarily stored in personal −20℃ freezers before being transported to the laboratory within a 24-hour timeframe. DNA extraction procedures were conducted in accordance with established protocols.

Metagenomic sequencing

The samples were sequenced on the NovaSeq 6000 platform with paired-end reads, an insert size of 350 bp, and a read length of 100 bp. Adaptor sequences and low-quality reads were removed from the raw data, and the remaining reads were filtered to exclude human host DNA via the human genome reference (hg18) as outlined in a previous study.[53] A total of 1,403.5 Gb of high-quality paired-end reads were obtained for the 132 samples, averaging 10.6 Gb per sample after the removal of human

DNA reads. The obtained sequences were deposited in the NCBI database (https://data view.ncbi.nlm.nih.gov/object/PRJNA1157583? reviewer=94q0mr5gq6ocslojevd04j420b and https://dataview.ncbi.nlm.nih.gov/object/ PRJNA1163867?reviewer=he36gb400guur438m j1o1j6jf7). We utilized the Integrated Gene Catalog of Gut Microbes (IGC) as the reference database for the gene set of human gut microbiota. Sequence alignment results exhibiting a similarity exceeding 90% were selected as the final alignment outcomes. Subsequently, we normalized the length information of each gene in the background database to obtain their relative abundances. For gene alignment, we utilized the Short Oligonucleotide Alignment Program (SOAP).

Subsequently, we annotated the genes obtained using the Kyoto Encyclopedia of Genes and Genomes (KEGG) annotation information corresponding to the IGC background database. These genes were then processed through computational algorithms to derive the relative abundance data of gene functions present in each sample. Further annotation of genes and KEGG Orthology (KO) terms was conducted utilizing several widely used databases, including Carbohydrate-Active enZyme (CAZy), Gut Metabolic Modules (GMMs), and Comprehensive Antibiotic Resistance Database (CARD), to ascertain the relative abundance of functional units at various levels. According to the official documentation of MetaPhlan3.0, we selected the recommended parameters for species annotation analysis and utilized the algorithm provided by the software to compute relative abundance information at the phylum, genus, and species levels. The MetaPhlan algorithm identifies unique clade-specific marker genes from approximately 17,000 reference genomes and subsequently compares them with pre-extracted marker genes using Bowtie2 to classify species and determine their relative abundance.

Trp metabolism

The participants' fecal samples were treated with an extract solution (1:10, w/v; methanol/acetonitrile/ water = 2:2:1, precooled at −40℃, containing 0.1% formic acid and an isotopically labeled internal standard mixture) and homogenized. Following centrifugation, the resulting supernatant (400 μl) was evaporated under N2, and then reconstituted with 100 μl of 0.1% formic acid. Subsequent centrifugation was performed to prepare samples for analysis. The target compounds were chromatographically separated using UHPLC with an ExionLC System (SCIEX) equipped with a Waters Acquity UPLC HSS T3 (100 × 2.1 mm, 1.8 μm) liquid chromatography column. The analysis utilized a SCIEX 6500 QTRAP+ triple quadrupole mass spectrometer with an IonDrive Turbo V electrospray ionization (ESI) interface, with specific parameter settings including curtain gas at 40 psi, IonSpray voltage at ±4500 V, temperature at 500℃, ion source gas 1 at 30 psi, and ion source gas 2 at 30 psi. Mass spectrum data acquisition and quantitative analysis of target compounds were conducted using SCIEX Analyst Work Station Software and SCIEX MultiQuant software.[54] Trp metabolism analysis was performed with the assistance of Shanghai Biotree Biotech Co.

Mice

Six-week-old female wild-type C57BL/6J (GemPharmatech, No. N000013) mice and four-week-old female BALB/c nude (GemPharmatech, No. D000521) mice were procured from the Model Animal Research Center of Nanjing University. The mice were housed in a controlled environment with independent ventilation systems, ensuring specific pathogen-free conditions, within the Animal Facility at Nanjing University. The researchers involved in the mouse experiment possessed valid animal breeding licenses.

Cell culture

The CRC cell lines HCT116 (ATCC, CCL-247) and MC38 (Kerafast, CVCL_B288) were procured from the Type Culture Collection of the Chinese Academy of Sciences in Shanghai, China. These cell lines were grown at 37℃ with 5% CO_2 in RPMI 1640 (Gibco, 11875500BT) supplemented with 10% heat-inactivated FBS (Celligent, CG0430B), and 1% antibiotic-antimycotic (Gibco 15,140–122). HCT116 and MC38 cells were seeded onto different types of plates and treated under

different conditions for further experiments when the cell density reached 80%. Dissolve the necessary pharmacological agents, including ILA (MCE HY-113099), CH223191 (MCE HY-12684), FICZ (MCE HY-12451), and 2-DG (MCE HY-13966), in DMSO. The experimental protocol ensures that the concentration of DMSO in the experimental group is equivalent to that in the control group. For the assessment of AHR functionality, cells were pre-treated with CH223191 (10 µM) for 4 hours prior to the administration of ILA (250 µM) and FICZ (100 nM). The experimental operators were blinded to the treatment conditions, with drug preparation conducted by separate personnel. The operators processed the cells based on their assigned numerical identifiers. All in vitro cell experiments involved a 12-hour starvation period using serum-free culture medium before cell stimulation.

In vivo animal studies

Each mouse was meticulously tagged with an ear tag for unique identification. Subsequently, by leveraging a random number table, the mice were randomly assigned to different experimental groups in strict accordance with the sequence of the randomly generated numbers. During the experimental process, a single – blind design was adopted, where only the experimental operators were kept unaware of the group assignments. Other dedicated personnel were solely responsible for drug preparation. The operators administered treatments to the mice strictly based on the assigned numbers.

In the xenograft model of CRC, 4-week-old female C57BL/6J (GemPharmatech, No. N000013) mice were subcutaneously injected with 1×10^6 MC38 cells, while 4-week-old female nude mice were subcutaneously injected with 5×10^6 HCT116 cells. The animals were randomized to treatment or control groups when tumors were palpable, at approximately 80 mm^3. ILA (400ug/20 g/d) was administered subcutaneously (s.c.) or intraperitoneally (i.p.) around the tumor every day,[8,22,55] while the control group received PBS subcutaneously. Tumor volume was measured and recorded throughout the experiment. The mice were euthanized using CO_2 inhalation when the tumors reached a final size of 1 cm^3, and the tumors were collected and weighed for further analysis. To induce colitis-associated CRC in C57BL/6J mice at 8 weeks of age, intraperitoneal injections of azoxymethane (AOM) at a dosage of 10 mg/kg were administered on day 1 ($n = 7$ per group). Following a 14-day interval, 2% dextran sulfate sodium (DSS) was added to the drinking water for 7 consecutive days, with three cycles of DSS treatment utilized. The mice were euthanized on day 120 after tumorigenesis induction. The administration of ILA commenced 10 days postinjection of AOM, either through oral ingestion by dissolving ILA in drinking water (p.o.) or intraperitoneally (i.p.) by dissolving ILA in PBS. Colon tissues, tumor tissues, feces, serum, spleens, and mesenteric lymph nodes (mLNs) were collected on day 120. Tumor number, tumor size, and total tumor mass (tumor load) were measured for each mouse. After they were macroscopically assessed, the colons were used for histopathological analysis.

Quantitative real-time PCR (qRT-PCR) and RNA-sequencing (RNA-seq)

TRIzol reagent (Vazyme, R411–01-AA) was utilized for the extraction of total RNA from the cell samples. Cytoplasmic and nuclear RNA were isolated using a Cytoplasmic & Nuclear RNA Purification Kit (Norgen Biotek, Thorold, ON, Canada) following the manufacturer's protocol. The extracted RNA was then reverse transcribed into cDNA using HiScript® III RT SuperMix (+gDNA wiper) (Vazyme, R223–01) for qRT-PCR analysis. The ABI StepOne Plus instrument with PowerUp™ SYBR® Green (Applied Biosystems, USA) was employed for the qRT-PCR analyses, with *Actin* serving as the internal control for normalization. A list of the qRT-PCR primers can be found in Table 1. For the RNA-seq experiments, isolated RNA samples were submitted to the BGI Genomics (Guangdong, China) for sequencing. The raw tag data were generated using the sequencing-by-synthesis methodology, and the institute subsequently processed the transcriptomic data. The raw data have been deposited in the Gene Expression Omnibus (GEO) under accession

Table 1. Reagents and tools table.

Reagent or Resource	Source	Identifier
Antibodies		
Rabbit monoclonal anti-HK2	ABclone	Cat# A0994 RRID: AB_2757513
Rabbit monoclonal anti-AHR	ABclone	A22464RRID: AB_3106896
Rabbit monoclonal anti-PFKL	Cell Signaling Technology	Cat#8175 RRID: AB_11178807
Rabbit monoclonal anti-PKM2	Cell Signaling Technology	Cat#4053 RRID: AB_1904096
Rabbit monoclonal anti-LDHA	Cell Signaling Technology	Cat#3582 RRID: AB_2066887
Rabbit monoclonal anti-CYP1B1	ABclone	Cat# A13967 RRID: AB_2760821
Rabbit monoclonal anti-BACH1	ABclone	Cat# A5393 RRID: AB_2766202
Rabbit monoclonal anti-NRF2	ABclone	Cat# A3577 RRID: AB_2941864
Mouse monoclonal anti-STAT3	Cell Signaling Technology	Cat#9139 RRID: AB_331757
Rabbit monoclonal anti-p-STAT3	Cell Signaling Technology	Cat#9145 RRID: AB_2491009
Rabbit monoclonal anti-β-ACTIN	Cell Signaling Technology	Cat#4970 RRID: AB_2223172
Anti-rabbit IgG, HRP-linked	Cell Signaling Technology	Cat#7074 RRID: AB_2099233
Anti-mouse IgG HRP-linked	Cell Signaling Technology	Cat#7076 RRID: AB_330924
ABflo® 488-conjugated Goat anti-RabbitIgG (H+L)	ABclone	Cat# AS073 RRID: AB_2768317
Rabbit monoclonal anti-Ki67	Cell Signaling Technology	Cat# 9027 RRID: AB_2636984
Rabbit monoclonal anti-PCNA	Cell Signaling Technology	Cat# 13110 RRID: AB_2636979
APC/Fire™ 750 anti-mouse CD45 Antibody	BioLegend	Cat# 147713 RRID: AB_2750440
PE anti-mouse/human CD11b Antibody	BioLegend	Cat# 101207 RRID: AB_312790
PE/Cyanine7 anti-mouse Gr-1 Antibody	BioLegend	Cat# 108415 RRID: AB_313380
FITC anti-mouse F4/80 Antibody	BioLegend	Cat# 123107 RRID: AB_893500
PE anti-mouse CD8a Antibody	BioLegend	Cat# 100707 RRID: AB_312746
APC anti-mouse CD3 Antibody	BioLegend	Cat# 100235 RRID: AB_2561455
FITC anti-mouse CD4 Antibody	BioLegend	Cat# 116003 RRID: AB_313688
Biological samples		
Colorectal cancer patient fecal	General Surgery Department, Nanjing Drum Tower Hospital	N/A
Healthy adult fecal	Physical Examination Center, Nanjing Drum Tower Hospital	N/A
Colorectal cancer patient tumor tissue	General Surgery Department, Nanjing Drum Tower Hospital	N/A
Colorectal cancer patient paratumor tissue	General Surgery Department, Nanjing Drum Tower Hospital	N/A
Chemicals, peptides, and recombinant proteins		
ILA	MCE	Cat# HY-113099
2-DG	MCE	Cat# HY-13966
CH223191	MCE	Cat# HY-12684
Phosphatase inhibitor	MCE	Cat# HY-K0023
Protease inhibitor	MCE	Cat# HY-K0010
RPMI Medium 1640	Gibco	Cat# 11875500BT
DMEM	Gibco	Cat# 11965092
Fetal Bovine Serum Standard	Gibco	Cat# CG0430B
Collagenase VIII	Sigma-aldrich	Cat# C2139
Collagenase IV	Sigma-aldrich	Cat#10780004
DNase I	Sigma-aldrich	Cat#10104159001
DMSO	Sigma-aldrich	Cat# D2650

(*Continued*)

Table 1. (Continued).

Reagent or Resource	Source	Identifier
Pen Strep	Gibco	Cat# 15140–122
0.25% Trypsin-EDTA	Gibco	Cat# 2509042
RIPA Lysis Buffer	Solarbio	Cat# R0010
Tween 20	Biosharp	Cat# 9005-64-5
BSA	Biofroxx	Cat# 9048-46-8
Crystal Violet Staining Sloution	Solarbio	Cat# G1062
Lipofectamine 3000	Thermo Fisher	Cat# L3000001
Triton X-100	Sigma-Aldrich	Cat# SLBT3016
Protein Ladder	ThermoFisher	Cat# 26617
Critical commercial assays		
EdU staining kitk (Fluor488)	KeyGEN	Cat# KGA9602–100
CCK8 Kit	Dojindo Laboratories	Cat# CK04
Annexin V FITC/PI Apoptosis Kit	Vazyme	Cat# A211–01
Enhanced ATP assay kit	Beyotime	Cat# S0027
Lactic Acid LD Detection Kit	KeyGEN	Cat# KGA7401–48
IHC kit	Beyotime	Cat# P0603
ChIP kit	BersinBio	Cat# Bes5001
BCA kit	Beyotime	Cat# P0010
ILA ELISA kit	KEQIAOBIO	Cat# KQ47423
Q RT SuperMix for qPCR	Vazyme	Cat# R223–01
Pro Universal SYBR Green qPCR Master Mix	Vazyme	Cat# Q712–02
Deposited data		
HCT116 RNA-seq	GEO	GSE271802
Human fecal metagenomics	NCBI	PRJNA1163867 and PRJNA1157583
Experimental models: Cell lines		
MC38	Kerafast	Cat# CVCL_B288
HCT116	ATCC	Cat# CCL-247
Experimental models: Organisms/strains		
Mouse: BALB/c nude mice	GemPharmatech Co., Ltd	BALB/cJGpt, Strain NO. N000521
Mouse: C57BL/6J mice	GemPharmatech Co., Ltd	C57BL/6JGpt, Strain NO. N000013
Oligonucleotides		
Primers for PDHA	This paper	N/A
Forward: TGGTAGCATCCCGTAATTTTGC		
Reverse: ATTCGGCGTACAGTCTGCATC		
Primers for PDHB	This paper	N/A
Forward: AAGAGGCGCTTTCACTGGAC		
Reverse: ACTAACCTTGTATGCCCCATCA		
Primers for CS	This paper	N/A
Forward: TGCTTCCTCCACGAATTTGAAA		
Reverse: CCACCATACATCATGTCCACAG		
Primers for ACO2	This paper	N/A
Forward: CCCTACAGCCTACTGGTGACT		
Reverse: TGTACTCGTTGGGCTCAAAGT		
Primers for IDH2	This paper	N/A
Forward: CGCCACTATGCCGACAAAAG		
Reverse: ACTGCCAGATAATACGGGTCA		
Primers for DLST	This paper	N/A
Forward: GAACTGCCCTCTAGGGAGAC		
Reverse:AACCTTCCTGCTGTTAGGGTA		
Primers for SDHB	This paper	N/A
Forward:ACAGCTCCCCGTATCAAGAAA		
Reverse:GCATGATCTTCGGAAGGTCAA		
Primers for SUCLG2	This paper	N/A
Forward:CAAAAGACCCTAATGTTGTGGGA		
Reverse:TTCAGCAACCATCACCTTGTT		
Primers for FH	This paper	N/A
Forward:GGAGGTGTGACAGAACGCAT		
Reverse:CATCTGCTGCCTTCATTATTGC		
Primers for HK2	This paper	N/A
Forward:GCCATCCTGCAACACTTAGGGCTTGAG		
Reverse:GTGAGGATGTAGCTTGTAGAGGGTCCC		
Primers for GPI	This paper	N/A
Forward:TATTGTGTTCACCAAGCTCACACC		
Reverse:TGGTAGAAGCGTCGTGAGAGGTC		

(*Continued*)

Table 1. (Continued).

Reagent or Resource	Source	Identifier
Primers for PFKL Forward:GGAGAAGCTGCGCGAGGTTTAC Reverse:ATTGTGCCAGCATCTTCAGCATGAG	This paper	N/A
Primers for ALDOA Forward:ATGCCCTACCAATATCCAGCA Reverse:GCTCCCAGTGGACTCATCTG	This paper	N/A
Primers for GAPDH Forward:TTCCGTGTCCCCACTGCCAACGT Reverse:CAAAGGTGGAGGAGTGGGTGTCGC	This paper	N/A
Primers for PGK1 Forward:ATGTCGCTTTCTAACAAGCTGA Reverse:GCGGAGGTTCTCCAGCA	This paper	N/A
Primers for PGAM1 Forward:GGAAACGTGTACTGATTGCAGCCC Reverse:TTCCATGGCTTTGCGCACCGTCT	This paper	N/A
Primers for ENO1 Forward: GACTTGGCTGGCAACTCTG Reverse: GGTCATCGGGAGACTTGAA	This paper	N/A
Primers for PKM2 Forward: ATGTCGAAGCCCCATAGTGAA Reverse: TGGGTGGTGAATCAATGTCCA	This paper	N/A
Primers for LDHA Forward: ATGGCAACTCTAAAGGATCA Reverse: GCAACTTGCAGTTCGGGC	This paper	N/A
Primers for β-actin Forward: CATGTACGTTGCTATCCAGGC Reverse: CTCCTTAATGTCACGCACGAT	This paper	N/A
shAHR Forward: gatccgCGGCATAGAGACCGACTTAATctcgagATTAAGTCGGTCTCTATGCCGtttttt Reverse: aattaaaaaaCGGCATAGAGACCGACTTAATctcgagATTAAGTCGGTCTCTATGCCGcg	This paper	N/A
Recombinant DNA		
Software and algorithms		
ImageJ	https://imagej.net/soft.ware/imagej/	RRID: SCR_003070
QuantStudio™ Real-Time PCR Software	https://www.thermofish.er.cn/cn/zh/home/glob.al/forms/life science/quantstudio-6-7-flex-software.html	RRID: SCR_020245
GraphPad Prism8	https://www.graphpad.com/features	RRID: SCR_002798
SlideViewer	https://www.3dhistech.com/research/software-downloads/	RRID: SCR_024885
Agilent Seahorse Wave	https://www.agilent.com/en/product/cell-analysis/real-time-cell-metabolic-analysis/xf-software/seahorse-wave-controller-software-2-6-1-740904.	RRID: SCR_024491
FlowJo	https://www.flowjo.com/solutions/flowjo.	RRID: SCR_008520
CytoFlex	https://www.beckman.com/flow-cytometry/instruments/cytoflex.	RRID: SCR_019627
PyMol	http://www.pymol.org/.	RRID:SCR_000305
Figdraw2.0	https://www.figdraw.com/.	N/A
Other		

number GSE271802 (https://www.ncbi.nlm.nih.gov/geo/query/acc.cgi?acc=GSE271802 secure token: efkricwqfnmbpen).

Western blotting (WB)

Tumor tissue was homogenized with three steel balls in lysis buffer (Solarbio, R0010) containing 1% phosphatase inhibitor (MCE, HY-K0023) and 1% protease inhibitor (MCE HY-K0010) in 200 µl of buffer per 20 mg of tissue. Proteins were extracted by centrifugation at 14,000 g for 20 minutes. Cell samples were treated with 200 µl of lysis buffer per 1×10^6 cells and centrifuged at 14,000 g for 20 minutes. Protein concentration was measured using a BCA kit (Beyotime, P0010). A total of 25 µg of protein per lane was separated on 8% and 12% polyacrylamide gels and transferred to polyvinylidene difluoride membranes. Membranes were blocked with 5% bovine serum albumin (Biofroxx 9048-46-8) in Tris-buffered saline with 0.1% Tween 20 (Biosharp 9005-64-5), then incubated with specific antibodies at 4℃ overnight. The next day, secondary antibodies were applied and visualized using an imaging system. Details of all relevant antibodies are provided in Table 1.

Plasmid construction and short hairpin RNA (shRNA) transfection

The human *HK2* sequence and *STAT3* sequence were synthesized by Corues Biotechnology (Nanjing, China) and subsequently subcloned into a pcDNA3.1 vector sourced from Addgene (Cambridge, MA) (Table S8). shRNAs targeting the AHR were procured from Corues Biotechnology, specifically shAHR no.1-TRCN0000021258, shAHR no.2-TRCN0000245285, and no.3-TRCN0000245286. Transfection of shAHR into cells was carried out using Lipofectamine 3000 (Thermo Fisher, L3000001）, and plasmid transfection was also conducted using the same reagent. Infections were performed in accordance with the manufacturer's instructions. Details of all relevant shRNA information are provided in Table 1.

Cell growth and proliferation assays

The cell growth rate was assessed via CCK-8 cell proliferation assays. Seven independent replicates of

MC38 and HCT116 cells treated with various conditions were incubated in 96-well plates. Subsequently, 10% CCK-8 solution (Dojindo Laboratories, CK04) was added to each well at specified time points, and the samples were incubated for an additional 2 hours. The absorbance of each well was measured at 450 nm. 5-Ethynyl-2'-deoxyuridine (EdU) assays were performed following the manufacturer's instructions via the EdU Cell Proliferation Assay Kit (KeyGEN, KGA9602–100). Cell colony formation was assessed via a colony formation assay, in which 1,000 cells were seeded in 6-well plates containing complete medium and incubated at 37°C in a 5% CO_2 environment for 2 weeks. Following fixation with methanol for 30 minutes, cells were stained with 0.2% crystal violet (Solarbio, G1062) solution, and colonies consisting of more than 50 cells were quantified.

Transwell assay

Cell migration assays were conducted with millicell cell culture inserts (24-well plates; 8 µm pore size; Merck KGaA, Darmstadt, Germany). MC38 and HCT116 cells were introduced into the upper chamber, while 1640 medium (600 µl) supplemented with 20% fetal bovine serum was added to the lower chamber. Following 24–48 hours of incubation, cells were fixed for 20 minutes with 4% paraformaldehyde, stained for 30 minutes with crystal violet (Solarbio, G1062), and subsequently imaged.

Flow cytometry analysis

Apoptosis was assessed through flow cytometric analysis via an Annexin V FITC/PI double-stain assay according to the manufacturer's instructions (Vazyme, A211–01). Flow cytometric analyses were performed via a CytoFlex (Beckman), and data interpretation was carried out via FlowJo software (Treestar, Inc., San Carlos). Tumor tissues were enzymatically digested with collagenase solution and subsequently filtered through a 200-mesh sieve to obtain a single-cell suspension. Details of all relevant antibodies are provided in Table 1.

Metabolite measurements

The concentrations of glucose and lactate in the medium were quantified separately using the

Glucose Assay Kit (Beyotime, S0201S) and the Lactate Colorimetric Assay Kit (KeyGEN, KGA7401–48), respectively, following the protocols provided by the manufacturers at the 24-hour time point. Intracellular ATP levels were measured using the Enhanced ATP Assay Kit (Beyotime, S2007). All metabolite measurements were conducted independently, with each assay performed a minimum of three times.

Seahorse metabolic analysis

Oxygen consumption rate (OCR) and extracellular acidification rate (ECAR) were measured with an Agilent Seahorse XFe96. The measurements were conducted employing the Seahorse XF Glycolysis Stress Test Kit (Agilent 103,020–100) and the Seahorse XFp Cell Mito Stress Test Kit (Agilent 103,010–100). Cells were subjected to a 12-hour starvation period in the absence of FBS, followed by treatment with 250 µM ILA for an additional 24 hours in a complete medium. Prior to each assay, the XFe96 cartridge was hydrated overnight in water within a no-CO$_2$ incubator maintained at 37℃. On the day of measurement, the water was replaced with pre-heated Seahorse XF Calibrant Solution (Agilent 100,840–000) and incubated for 90 minutes. The cell medium was subsequently removed and replaced with 180 µL per well of Agilent Seahorse XF RPMI Medium at pH 7.4 (Agilent 103,681–100), and the cells were incubated for 1 hour in a no-CO$_2$ incubator at 37℃. Following this preparation, the medication was added according to the instructions provided in the kit.

Immunohistochemistry (IHC)

Immunohistochemistry (IHC) was conducted according to established protocols,[56] involving rehydration of tumor tissue slides, antigen retrieval, blocking, and incubation with primary antibodies. Subsequently, secondary antibodies were applied and the slides were stained using an IHC kit (Beyotime, P0603), with DAB peroxidase substrate. Details of all relevant antibodies' information are provided in Table 1.

Chromatin immunoprecipitation (ChIP) assay

Chromatin immunoprecipitation (ChIP) assay was performed following the instructions provided by the manufacturer via a ChIP Assay Kit (BersinBio, Bes5001). HCT116 cells were treated with 1% formaldehyde for 10 minutes at room temperature to cross-link proteins and DNA. The cross-linking reaction was stopped by the addition of a stop-fix solution containing glycine (125 mm), aprotinin (1 µg/ml), pepstatin A (1 µg/ml), and Pefabloc (1 mg/ml) for 5 minutes at room temperature. The samples were then centrifuged at 2,500 × g and 4°C for 2 minutes, washed with ice-cold PBS, and subjected to chromatin immunoprecipitation using IgG (BersinBio) and anti-STAT3 (Cell Signaling Technology, 9139) antibodies. The association of STAT3 with *HK2* promoter was measured by ChIP-PCR with the following primers: forward, 5'-GCACTGGTGGAGAATGGCAAG-3', and reverse, 5'-CTGTACACATTGCAGACAGCACC-3'.

Molecular docking

To obtain the three-dimensional structure of ILA, access PubChem (https://pubchem.ncbi.nlm.nih.gov) and export the structure using PyMol. The phosphorylated dimer crystal structure of STAT3 is available under PDB ID: 4e68. According to the literature, phosphorylated Tyr705 (pTyr705) binds to the SH2 domain.[39] Therefore, PyMol was utilized to isolate and export the SH2 domain for subsequent protein-ligand docking studies. According to literature reports, the pTyr705 binding pocket position was utilized as the substrate docking site.[39] Indole lactate and SH2 were subjected to 100 docking simulations using AutoDock, with the lowest energy conformation being selected as the output structure. The interaction forces between ILA and SH2 were subsequently analyzed using PyMol.

Data source

RNA-sequencing expression profiles (level 3) and associated clinical data for colorectal cancer (CRC) were obtained from The Cancer Genome Atlas

(TCGA) dataset (https://portal.gdc.cancer.gov). Additionally, the GSE24550 dataset was retrieved from the Gene Expression Omnibus (GEO) database (http://www.ncbi.nlm.nih.gov/geo). The raw data were acquired in MINiML file format. RNA sequencing data acquisition address: https://www.ncbi.nlm.nih.gov/geo/query/acc.cgi?acc=GSE271802.

Quantification and statistical analysis

The data presented in this study are displayed as the mean ± SD, unless otherwise specified, and are elaborated upon in the corresponding section of the methodology and figure legend. An unpaired, two-tailed t-test was used to compare two sample sets that adhered to a normal distribution and homogeneity of variance. When sample sets deviated from normality and variance, or when normality and variance could not be assessed, the Mann–Whitney U-test was used. The Mann–Whitney U-test was also used for pairwise comparisons involving three or more samples. The Pearson correlation test was used to analyze correlations between two continuous variables. The Benjamini–Hochberg (BH) method was used to correct for multiple testing in the analysis of metagenomic sequencing, metabolomics, and RNA-seq data. Specific statistical methods are described in the corresponding figure legends. The p values were calculated using either SPSS 26.0 or GraphPad Prism 9.0, with significance levels denoted as follows: $^*p < 0.05$, $^{**}p < 0.01$, $^{***}p < 0.001$, and ns indicating no significance. Details of the bioinformatics analyses are provided in the aforementioned sections.

Highlights

- The intestinal levels of indole-3-lactic acid (ILA) are markedly reduced in patients with colorectal cancer, and this deficiency is significantly associated with tumor progression.
- Exogenous administration of ILA inhibits colorectal cancer development both in vitro and in vivo. ILA exerts a direct effect on tumor cells, inhibiting their proliferation, migration, and antiapoptotic capabilities.
- ILA directly inhibits the p-STAT3/HK2 pathway, independent of the aryl hydrocarbon receptor, thereby reprogramming tumor cell glucose metabolism and suppressing the Warburg effect.

Acknowledgments

Disclosure statement

No potential conflict of interest was reported by the author(s).

Funding

ORCID

Shizhen Zhou 🔘 http://orcid.org/0000-0001-8678-9855

Author contributions

T.W., W.G., and C.D. conceptualized the study and supervised the data analysis; S.Z. conceived and supervised the whole project, interpreted the data, and wrote the manuscript; K.W. performed WB experiments; L.L, J. M., Q.Y., and H.W. collected clinical samples and organized clinical data; X.Z. developed animal models and performed the experiments; J. H., Z. W. contributed to the analysis tools and analyzed the data.

Ethics statement

All participants provided informed consent, and the human sample study received approval from the Ethics Committee of Nanjing Drum Tower Hospital (No.2022-496-02). Approval for all mouse experiments was obtained from the Review Committee of Nanjing Drum Tower Hospital (No.2024AE01020).

References

1. Siegel RL, Giaquinto AN, Jemal A. Cancer statistics, 2024. CA Cancer J Clin. 2024;74(1):12–49. doi: 10.3322/caac.21820.
2. Eng C, Yoshino T, Ruíz-García E, Mostafa N, Cann CG, O'Brian B, Benny A, Perez RO, Cremolini C. Colorectal cancer. Lancet. 2024;404(10449):294–310. doi: 10.1016/s0140-6736(24)00360-x.

3. Cui W, Guo M, Liu D, Xiao P, Yang C, Huang H, Liang C, Yang Y, Fu X, Zhang Y, et al. Gut microbial metabolite facilitates colorectal cancer development via ferroptosis inhibition. Nat Cell Biol. 2024;26 (1):124–137. doi: 10.1038/s41556-023-01314-6.

4. Qu R, Zhang Y, Ma Y, Zhou X, Sun L, Jiang C, Zhang Z, Fu W. Role of the gut microbiota and its metabolites in Tumorigenesis or development of colorectal cancer. Adv Sci (Weinh). 2023;10(23):e2205563. doi: 10.1002/advs.202205563.

5. Janney A, Powrie F, Mann EH. Host–microbiota maladaptation in colorectal cancer. Nature. 2020;585 (7826):509–517. doi: 10.1038/s41586-020-2729-3.

6. Wong CC, Yu J. Gut microbiota in colorectal cancer development and therapy. Nat Rev Clin Oncol. 2023;20 (7):429–452. doi: 10.1038/s41571-023-00766-x.

7. Hou H, Chen D, Zhang K, Zhang W, Liu T, Wang S, Dai X, Wang B, Zhong W, Cao H. Gut microbiota-derived short-chain fatty acids and colorectal cancer: ready for clinical translation? Cancer Lett. 2022;526:225–235. doi: 10.1016/j.canlet.2021.11.027.

8. Zhang Q, Zhao Q, Li T, Lu L, Wang F, Zhang H, Liu Z, Ma H, Zhu Q, Wang J, et al. Lactobacillus plantarum-derived indole-3-lactic acid ameliorates colorectal tumorigenesis via epigenetic regulation of CD8+ T cell immunity. Cell Metab. 2023;35(6):943–960.e949. doi: 10.1016/j.cmet.2023.04.015.

9. Jia D, Wang Q, Qi Y, Jiang Y, He J, Lin Y, Sun Y, Xu J, Chen W, Fan L, et al. Microbial metabolite enhances immunotherapy efficacy by modulating T cell stemness in pan-cancer. Cell. 2024;187(7):1651–1665.e1621. doi: 10.1016/j.cell.2024.02.022.

10. Sobhani I, Bergsten E, Couffin S, Amiot A, Nebbad B, Barau C, De'angelis N, Rabot S, Canoui-Poitrine F, Mestivier D, et al. Colorectal cancer-associated microbiota contributes to oncogenic epigenetic signatures. Proc Natl Acad Sci USA. 2019;116(48):24285–24295. doi: 10.1073/pnas.1912129116.

11. Chen A, Jiang Z, Cai L, Tang D. On the road to colorectal cancer development: crosstalk between the gut microbiota, metabolic reprogramming, and epigenetic modifications. Carcinogenesis. 2023;44(8–9):631–641. doi: 10.1093/carcin/bgad058.

12. Chen D, Jin D, Huang S, Wu J, Xu M, Liu T, Dong W, Liu X, Wang S, Zhong W, et al. Clostridium butyricum, a butyrate-producing probiotic, inhibits intestinal tumor development through modulating wnt signaling and gut microbiota. Cancer Lett. 2020;469:456–467. doi: 10.1016/j.canlet.2019.11.019.

13. Sipe LM, Chaib M, Pingili AK, Pierre JF, Makowski L. Microbiome, bile acids, and obesity: how microbially modified metabolites shape anti-tumor immunity. Immunological Rev. 2020;295(1):220–239. doi: 10.1111/imr.12856.

14. Bell HN, Rebernick RJ, Goyert J, Singhal R, Kuljanin M, Kerk SA, Huang W, Das NK, Andren A, Solanki S, et al. Reuterin in the healthy gut microbiome suppresses colorectal cancer growth through altering redox balance. Cancer Cell. 2022;40(2):185–200.e186. doi: 10.1016/j.ccell.2021.12.001.

15. Konishi H, Fujiya M, Tanaka H, Ueno N, Moriichi K, Sasajima J, Ikuta K, Akutsu H, Tanabe H, Kohgo Y. Probiotic-derived ferrichrome inhibits colon cancer progression via JNK-mediated apoptosis. Nat Commun. 2016;7(1):12365. doi: 10.1038/ncomms12365.

16. Bender MJ, McPherson AC, Phelps CM, Pandey SP, Laughlin CR, Shapira JH, Medina Sanchez L, Rana M, Richie TG, Mims TS, et al. Dietary tryptophan metabolite released by intratumoral lactobacillus reuteri facilitates immune checkpoint inhibitor treatment. Cell. 2023;186(9):1846–1862.e1826. doi: 10.1016/j.cell.2023.03.011.

17. Roager HM, Licht TR. Microbial tryptophan catabolites in health and disease. Nat Commun. 2018;9(1):3294. doi: 10.1038/s41467-018-05470-4.

18. Hezaveh K, Shinde RS, Klötgen A, Halaby MJ, Lamorte S, Ciudad MT, Quevedo R, Neufeld L, Liu ZQ, Jin R, et al. Tryptophan-derived microbial metabolites activate the aryl hydrocarbon receptor in tumor-associated macrophages to suppress anti-tumor immunity. Immunity. 2022;55(2):324–340.e8. doi: 10.1016/j.immuni.2022.01.006.

19. Yu K, Li Q, Sun X, Peng X, Tang Q, Chu H, Zhou L, Wang B, Zhou Z, Deng X, et al. Bacterial indole-3-lactic acid affects epithelium–macrophage crosstalk to regulate intestinal homeostasis. Proc Natl Acad Sci USA. 2023;120(45):e2309032120. doi: 10.1073/pnas.2309032120.

20. Huang W, Cho KY, Meng D, Walker WA. The impact of indole-3-lactic acid on immature intestinal innate immunity and development: a transcriptomic analysis. Sci Rep. 2021;11(1):8088. doi: 10.1038/s41598-021-87353-1.

21. Ehrlich AM, Pacheco AR, Henrick BM, Taft D, Xu G, Huda MN, Mishchuk D, Goodson ML, Slupsky C, Barile D, et al. Indole-3-lactic acid associated with Bifidobacterium-dominated microbiota significantly decreases inflammation in intestinal epithelial cells. BMC Microbiol. 2020;20(1):357. doi: 10.1186/s12866-020-02023-y.

22. Zhang S, Nie Q, Sun Y, Zuo S, Chen C, Li S, Yang J, Hu J, Zhou X, Yu Y, et al. Bacteroides uniformis degrades β-glucan to promote lactobacillus johnsonii improving indole-3-lactic acid levels in alleviating colitis. Microbiome. 2024;12(1):177. doi: 10.1186/s40168-024-01896-9.

23. Sugimura N, Li Q, Chu ESH, Lau HCH, Fong W, Liu W, Liang C, Nakatsu G, Su ACY, Coker OO, et al. Lactobacillus gallinarum modulates the gut microbiota and produces anti-cancer metabolites to protect against colorectal tumourigenesis. Gut. 2021;71 (10):2011–2021. doi: 10.1136/gutjnl-2020-323951.

24. Wang L, Tu YX, Chen L, Yu KC, Wang HK, Yang SQ, Zhang Y, Zhang SJ, Song S, Xu HL, et al. Black rice diet

alleviates colorectal cancer development through modulating tryptophan metabolism and activating AHR pathway. Imeta. 2024;3:e165. doi: 10.1002/imt2.165.

25. Xu H, Wang Y, Liu G, Zhu Z, Shahbazi MA, Reis RL, Kundu SC, Shi X, Zu M, Xiao B. Nano-armed Limosilactobacillus reuteri for enhanced photo-immunotherapy and microbiota tryptophan metabolism against colorectal cancer. Adv Sci (Weinh). 2024;12(7):e2410011. doi: 10.1002/advs. 202410011.

26. Zhong X, He X, Wang Y, Hu Z, Huang H, Zhao S, Wei P, Li D. Warburg effect in colorectal cancer: the emerging roles in tumor microenvironment and therapeutic implications. J Hematol & Oncol. 2022;15 (1):160. doi: 10.1186/s13045-022-01358-5.

27. Liao M, Yao D, Wu L, Luo C, Wang Z, Zhang J, Liu B. Targeting the Warburg effect: a revisited perspective from molecular mechanisms to traditional and innovative therapeutic strategies in cancer. Acta Pharm Sin B. 2024;14(3):953–1008. doi: 10.1016/j.apsb.2023.12.003.

28. Sun M, Ma N, He T, Johnston LJ, Ma X. Tryptophan (trp) modulates gut homeostasis via aryl hydrocarbon receptor (AhR). Crit Rev Food Sci Nutr. 2020;60 (10):1760–1768. doi: 10.1080/10408398.2019.1598334.

29. Meng D, Sommella E, Salviati E, Campiglia P, Ganguli K, Djebali K, Zhu W, Walker WA. Indole-3-lactic acid, a metabolite of tryptophan, secreted by Bifidobacterium longum subspecies infantis is anti-inflammatory in the immature intestine. Pediatr Res. 2020;88(2):209–217. doi: 10.1038/s41390-019-0740-x.

30. Lian J, Lin H, Zhong Z, Song Y, Shao X, Zhou J, Xu L, Sun Z, Yang Y, Chi J, et al. Indole-3-lactic acid inhibits doxorubicin-induced Ferroptosis through activating aryl hydrocarbon Receptor/Nrf2 signalling pathway. J Cell Mol Med. 2025;29(2):e70358. doi: 10.1111/jcmm.70358.

31. Opitz CA, Holfelder P, Prentzell MT, Trump S. The complex biology of aryl hydrocarbon receptor activation in cancer and beyond. Biochem Pharmacol. 2023;216:115798. doi: 10.1016/j.bcp.2023.115798.

32. Kwon YJ, Shin S, Chun YJ. Biological roles of cytochrome P450 1A1, 1A2, and 1B1 enzymes. Arch Pharm Res. 2021;44(1):63–83. doi: 10.1007/s12272-021-01306-w.

33. Zhao B, Degroot DE, Hayashi A, He G, Denison MS. CH223191 is a ligand-selective antagonist of the ah (dioxin) receptor. Toxicological Sci: An Off J Soc Toxicol. 2010;117(2):393–403. doi: 10.1093/toxsci/kfq217.

34. Li YJ, Zhang C, Martincuks A, Herrmann A, Yu H. STAT proteins in cancer: orchestration of metabolism. Nat Rev Cancer. 2023;23(3):115–134. doi: 10.1038/s41568-022-00537-3.

35. Zou S, Tong Q, Liu B, Huang W, Tian Y, Fu X. Targeting STAT3 in cancer immunotherapy. Mol

Cancer. 2020;19(1):145. doi: 10.1186/s12943-020-01258-7.

36. Sgrignani J, Garofalo M, Matkovic M, Merulla J, Catapano CV, Cavalli A. Structural biology of STAT3 and its implications for anticancer therapies development. IJMS. 2018;19(6):1591. doi: 10.3390/ijms19061591.

37. Lin WH, Chang YW, Hong MX, Hsu TC, Lee KC, Lin C, Lee JL. STAT3 phosphorylation at Ser727 and Tyr705 differentially regulates the EMT–MET switch and cancer metastasis. Oncogene. 2021;40(4):791–805. doi: 10.1038/s41388-020-01566-8.

38. Chalikonda G, Lee H, Sheik A, Huh YS. Targeting key transcriptional factor STAT3 in colorectal cancer. Mol Cellular Biochem. 2021;476(9):3219–3228. doi: 10.1007/s11010-021-04156-8.

39. Dong J, Cheng XD, Zhang WD, Qin JJ. Recent update on development of small-molecule STAT3 inhibitors for cancer therapy: from phosphorylation inhibition to protein degradation. J Med Chem. 2021;64 (13):8884–8915. doi: 10.1021/acs.jmedchem.1c00629.

40. He P, Miao Y, Sun Y, Bian A, Jin W, Chen H, Ye J, He J, Peng Y, Gu H, et al. Discovery of a novel potent STAT3 inhibitor HP590 with dual p-tyr 705 /Ser 727 inhibitory activity for gastric cancer treatment. J Med Chem. 2022;65(19):12650–12674. doi: 10.1021/acs.jmedchem.2c00413.

41. Fornes O, Castro-Mondragon JA, Khan A, van der Lee R, Zhang X, Richmond PA, Modi BP, Correard S, Gheorghe M, Baranašić D, et al. JASPAR 2020: update of the open-access database of transcription factor binding profiles. Nucleic Acids Res. 2020;48:D87–d92. doi: 10.1093/nar/gkz1001.

42. Sorbara MT, Pamer EG. Microbiome-based therapeutics. Nat Rev Microbiol. 2022;20(6):365–380. doi: 10.1038/s41579-021-00667-9.

43. Zhang H, Xu H, Zhang C, Tang Q, Bi F. Ursodeoxycholic acid suppresses the malignant progression of colorectal cancer through TGR5-YAP axis. Cell Death Discov. 2021;7(1):207. doi: 10.1038/s41420-021-00589-8.

44. Tian Y, Gui W, Koo I, Smith PB, Allman EL, Nichols RG, Rimal B, Cai J, Liu Q, Patterson AD. The microbiome modulating activity of bile acids. Gut Microbes. 2020;11(4):979–996. doi: 10.1080/19490976.2020.1732268.

45. Tao S, Wang Y, Yu C, Qiu R, Jiang Y, Jia J, Tao Z, Zhang L, Zou B, Tang D. Gut microbiota mediates the inhibition of lymphopoiesis in dietary-restricted mice by suppressing glycolysis. Gut Microbes. 2022;14 (1):2117509. doi: 10.1080/19490976.2022.2117509.

46. Zhang X, Wu L, Xu Y, Yu H, Chen Y, Zhao H, Lei J, Zhou Y, Zhang J, Wang J, et al. Microbiota-derived SSL6 enhances the sensitivity of hepatocellular carcinoma to sorafenib by down-regulating glycolysis. Cancer Lett. 2020;481:32–44. doi: 10.1016/j.canlet.2020.03.027.

47. Stine ZE, Schug ZT, Salvino JM, Dang CV. Targeting cancer metabolism in the era of precision oncology. Nat Rev Drug Discov. 2022;21(2):141–162. doi: 10.1038/s41573-021-00339-6.

48. Wang A, Guan C, Wang T, Mu G, Tuo Y. Lactiplantibacillus plantarum-derived indole-3-lactic acid ameliorates intestinal barrier integrity through the AhR/Nrf2/NF-κB Axis. J Agric Food Chem. 2024; doi: 10.1021/acs.jafc.4c01622.

49. Trikha P, Lee DA. The role of AhR in transcriptional regulation of immune cell development and function. Biochim Biophys Acta Rev Cancer. 2020;1873 (1):188335. doi: 10.1016/j.bbcan.2019.188335.

50. Shinde R, McGaha TL. The aryl hydrocarbon receptor: connecting immunity to the microenvironment. Trends Immunol. 2018;39(12):1005–1020. doi: 10.1016/j.it.2018.10.010.

51. Fiore A, Zeitler L, Russier M, Groß A, Hiller MK, Parker JL, Stier L, Köcher T, Newstead S, Murray PJ. Kynurenine importation by SLC7A11 propagates anti-ferroptotic signaling. Mol Cell. 2022;82(5):920–932.e927. doi: 10.1016/j.molcel.2022.02.007.

52. Sun L, Li X, Xiao Y, Yu W, Chen X, Wang Z, Xia N, Chen X, Chen M, Zhu H, et al. Mfsd2a suppresses colorectal cancer progression and liver metastasis via the S100A14/STAT3 axis. J Transl Med. 2025;23(1):59. doi: 10.1186/s12967-024-05994-y.

53. Li J, Jia H, Cai X, Zhong H, Feng Q, Sunagawa S, Arumugam M, Kultima JR, Prifti E, Nielsen T, et al. An integrated catalog of reference genes in the human gut microbiome. Nat Biotechnol. 2014;32(8):834–841. doi: 10.1038/nbt.2942.

54. Hu S, Luo L, Bian X, Liu RH, Zhao S, Chen Y, Sun K, Jiang J, Liu Z, Zeng L. Pu-erh tea restored circadian rhythm disruption by regulating tryptophan metabolism. J Agric Food Chem. 2022;70 (18):5610–5623. doi: 10.1021/acs.jafc.2c01883.

55. Li Y, Li Q, Yuan R, Wang Y, Guo C, Wang L. Bifidobacterium breve-derived indole-3-lactic acid ameliorates colitis-associated tumorigenesis by directing the differentiation of immature colonic macrophages. Theranostics. 2024;14(7):2719–2735. doi: 10.7150/thno.92350.

56. Wang X, Chen Q, Bing Z, Zhou S, Xu Z, Hou Y, Zhao Y, Zhao S, Wang T. Low expression of m6A reader YTHDC1 promotes progression of ovarian cancer via PIK3R1/STAT3/GANAB axis. Int J Biol Sci. 2023;19(14):4672–4688. doi: 10.7150/ijbs.81595.